



Resolving glacial isostatic adjustment (GIA) in response to modern and future ice loss at marine grounding lines in West Antarctica

Jeannette Xiu Wen Wan¹, Natalya Gomez¹, Konstantin Latychev², and Holly Kyeore Han^{1,3}

¹Department of Earth and Planetary Sciences, McGill University, Montreal, Canada

²Department of Earth and Planetary Sciences, Harvard University, Cambridge, Massachusetts, USA

³Fluid Dynamics and Solid Mechanics Group, Los Alamos National Laboratory, Los Alamos, USA

Correspondence: Natalya Gomez (natalya.gomez@mcgill.ca)

Received: 29 July 2021 – Discussion started: 11 August 2021

Revised: 21 January 2022 – Accepted: 30 January 2022 – Published: 13 June 2022

Abstract. Accurate glacial isostatic adjustment (GIA) modelling in the cryosphere is required for interpreting satellite, geophysical and geological records and for assessing the feedbacks of Earth deformation and sea-level change on marine ice-sheet grounding lines. GIA modelling in areas of active ice loss in West Antarctica is particularly challenging because the ice is underlain by laterally varying mantle viscosities that are up to several orders of magnitude lower than the global average, leading to a faster and more localised response of the solid Earth to ongoing and future ice-sheet retreat and necessitating GIA models that incorporate 3-D viscoelastic Earth structure. Improvements to GIA models allow for computation of the viscoelastic response of the Earth to surface ice loading at sub-kilometre resolution, and ice-sheet models and observational products now provide the inputs to GIA models at comparably unprecedented detail. However, the resolution required to accurately capture GIA in models remains poorly understood, and high-resolution calculations come at heavy computational expense. We adopt a 3-D GIA model with a range of Earth structure models based on recent seismic tomography and geodetic data to perform a comprehensive analysis of the influence of grid resolution on predictions of GIA in the Amundsen Sea Embayment (ASE) in West Antarctica. Through idealised sensitivity testing down to sub-kilometre resolution with spatially isolated ice loading changes, we find that a grid resolution of $\sim \frac{1}{3}$ of the radius of the load or higher is required to accurately capture the elastic response of the Earth. However, when we consider more realistic, spatially coherent ice loss scenarios based on modern observational records and future ice-sheet model projections and adopt a viscoelastic Earth, we find that predicted defor-

mation and sea-level change along the grounding line converge to within 5 % with grid resolutions of 7.5 km or higher, and to within 2 % for grid resolutions of 3.75 km and higher, even when the input ice model is on a 1 km grid. Furthermore, we show that low mantle viscosities beneath the ASE lead to viscous deformation that contributes to the instrumental record on decadal timescales and equals or dominates over elastic effects by the end of the 21st century. Our findings suggest that for the range of resolutions of 1.9–15 km that we considered, the error due to adopting a coarser grid in this region is negligible compared to the effect of neglecting viscous effects and the uncertainty in the adopted mantle viscosity structure.

1 Introduction

Changes in sea level in response to ice-mass loss are spatially variable because of glacial isostatic adjustment (GIA), the deformational, gravitational and rotational response of the Earth to changes in surface ice and water distribution. The response of the bedrock is viscoelastic, beginning with an instantaneous elastic response of the solid planet's lithosphere and mantle and transitioning to a longer timescale viscous relaxation of the mantle towards isostatic equilibrium. GIA models produce predictions of changes in the height of the sea surface equipotential and solid Earth surface (i.e. sea-level changes) in response to surface ice and water loading changes, which are in turn used to interpret satellite, geophysical and geological records and serve as input to models of ice-sheet dynamics.

Accurate GIA modelling is required to constrain the sea-level and solid Earth feedbacks on ice dynamics in the coming centuries, especially along unstable marine-grounded ice fronts in Antarctica where bedrock uplift and gravitational drawdown of the sea surface due to ice loss act as a negative feedback to stabilise the retreat of marine-grounded ice-sheet grounding lines (e.g. Gomez et al., 2010, 2013, 2015; De Boer et al., 2014; Konrad et al., 2015; Larour et al., 2019). Furthermore, the Earth's response to past and modern ice cover changes makes a significant contribution to satellite records of modern mass changes in marine sectors of West Antarctica that are actively experiencing ice loss (e.g. King et al., 2012; the IMBIE team, 2018).

GIA modelling in Antarctica is complicated by the fact that the continent is characterised by strong lateral variability in lithospheric thickness and upper-mantle viscosity, with low viscosities in the west and high viscosities in the east (e.g. An et al., 2015a; Heeszel et al., 2016; Lloyd et al., 2020). In particular, the low-viscosity mantle and thin lithosphere observed under the West Antarctic Ice Sheet (WAIS) identified from increasingly resolved seismic tomography and geodetic and geologic constraints (Ritzwoller et al., 2001; Morelli and Danesi, 2004; Kaufmann et al., 2005; Nield et al., 2014; Heeszel et al., 2016; Barletta et al., 2018; Shen et al., 2018; Lloyd et al., 2020) lead to a more spatially localised (short wavelength) and faster viscoelastic response to surface loading than cratonic regions covered by Late Pleistocene ice sheets (e.g. Hay et al., 2017; Powell et al., 2020). Over West Antarctica, upper-mantle viscosities are thought to vary by several orders of magnitude over short spatial scales (\sim hundreds of kilometres) reaching as low as 10^{18} Pa s in the Amundsen Sea Embayment (ASE) beneath areas of active marine ice loss (e.g. Nield et al., 2014; Barletta et al., 2018). This implies that viscous effects due to 20th century and more recent ice loss will become significant on annual to decadal timescales and accelerate during the time frame of instrumental records (Barletta et al., 2018; Powell et al., 2020). Viscous deformation due to ongoing ice loss also has the potential to influence ice-sheet grounding lines in the coming centuries (Gomez et al., 2015; Kachuck et al., 2020; Coulson et al., 2021) but has not been included in recent high-resolution coupled ice-sheet–sea-level model projections (Larour et al., 2019).

To accurately capture the timing and wavelength of GIA effects across Antarctica, models must be capable of both accounting for 3-D Earth structure (i.e. 3-D GIA models such as Latychev et al., 2005, or van der Wal et al., 2015) and be of sufficient spatiotemporal resolution to capture the geometry of grounded ice cover (e.g. Han et al., 2022). Commonly, GIA, ice-sheet and coupled ice-sheet–GIA modelling (e.g. Gomez et al., 2015; Konrad et al. 2015) studies that consider modern and future ice-sheet changes have been performed with only 1-D (radially varying) Earth structure models (e.g. Kendall et al., 2005; Spada and Stocchi, 2007; Adhikari et al., 2016) or with coarse spatial resolutions of > 20 km

due to the computational expense. GIA models capable of kilometre to sub-kilometre resolution have also been developed (e.g. the 1-D GIA model by Adhikari et al., 2016; the 3-D GIA model by Latychev et al., 2005, with updates described in the Supplement of Gomez et al., 2018). For computational efficiency, some of these models implement regional grid refinement techniques which allow for a higher resolution along ice retreat margins. Alongside this, improvements in ice-sheet models (e.g. Nowicki et al., 2016; Seroussi et al., 2020; DeConto et al., 2021) and observational products (e.g. Studinger, 2014; Bamber et al., 2020; Smith et al., 2020; Morlinghem et al., 2020) have been made to provide similarly high-resolution (kilometre to sub-kilometre) ice thickness and bedrock topography datasets that serve as input to GIA models. These advancements together allow for GIA models to capture short-wavelength bedrock deformation and input ice loading changes at unprecedented detail but at still heavy computational expense, particularly for global 3-D GIA models.

It is well-established that dynamic ice-sheet models are sensitive to the chosen grid resolution (e.g. Durand et al., 2009; Van den Berg and Van de Wal, 2006), requiring kilometre to sub-kilometre resolution to accurately represent ice dynamics and grounding-line migration in some applications (e.g. Gladstone et al., 2012; Pattyn et al., 2013; Cornford et al., 2016). It has also been suggested that bedrock topography as fine as 1 km resolution may be needed to capture the influence of fine-scale topographic features on the ice-sheet evolution (Durand et al., 2009), and high resolution may also be needed to represent some embayment walls and pinning points that act to slow down retreat (e.g. Favier et al., 2012; Jougin et al., 2014; Berger et al., 2016).

While topographic features themselves can be very fine scale, the changes in bedrock elevation and sea level in response to ice cover changes tend to be longer wavelength, and the corresponding spatial resolution required to accurately resolve these changes in GIA models and their influence on ice dynamics remains poorly understood. Larour et al. (2019) suggested that kilometre-scale resolution may be required to capture the elastic component of deformation in response to ice loss. However, the idealised tests they performed considered an isolated and increasingly localised load, and their conclusion may not hold for more realistic, spatially coherent ice loss scenarios. Furthermore, their model did not include viscous deformation in response to ongoing ice loss during the simulation or account for lateral variations in Earth structure. There have been limited studies assessing the length scale of realistic viscoelastic bedrock response in the rheologically complex region beneath the WAIS, though a recent high-resolution bedrock deformation modelling study by Zwinger et al. (2020) suggests a convergence in modelled viscoelastic deformation at resolutions finer than 5 km. The broad spatial nature of bedrock deformation and the spatially coherent nature of ice-sheet retreat, which becomes less localised over longer timescales, suggest

that sub-kilometre to kilometre grid resolution, which comes at great computational cost, may not be necessary for accurate GIA model calculations.

The aim of this study is to assess the sensitivity of GIA model predictions of Earth deformation and sea-level change in response to modern and future ice loss to spatial resolution in the rheologically complex marine sectors of the WAIS. We build a 3-D viscosity model based on the most recent Antarctic-wide seismic tomography model (Lloyd et al., 2020) to serve as input to a 3-D finite volume, global GIA model (Latychev et al., 2005) to assess the performance of 3-D GIA model predictions across surface grid resolutions of 1.9–15 km. We repeat calculations with a range of Earth models, considering the contribution from elastic and viscous deformation separately. We focus on the response to observed modern ice loss over the last two decades (Shepherd et al., 2019) and projected future ice-sheet retreat in the coming century (Golledge et al., 2019; DeConto et al., 2021) in the Amundsen Sea Embayment of West Antarctica. Our study is motivated by the following questions. What 3-D grid resolution is necessary to adequately capture the elastic and viscous deformation and sea-level changes in response to ice loading changes? How significant is the effect of grid resolution compared to sources of uncertainty and simplifications made in some previous modelling, in particular the neglect of viscous deformation?

2 Methods

To investigate the influence of GIA model grid resolution, we first conduct idealised load sensitivity tests over a range of surface grid resolutions from 7.5 to 0.5 km for the instantaneous removal of cylindrical loads from 0.5 to 16 km in radius (Sect. 3). We then widen our “aperture” to assess the model grid resolution required to accurately capture GIA due to modern ice cover changes from satellite observations (Shepherd et al., 2019) and projected ice loss from ice-sheet models (Golledge et al., 2019; DeConto et al., 2021) in the rapidly evolving Amundsen Sea Embayment of West Antarctica (Sect. 4). We choose to locate our study region (light blue square in Fig. 1a) on the ASE both because of the ongoing ice loss and vulnerability of marine-based ice sheets to large-scale retreat in the region and because the region is characterised by low upper-mantle viscosities and a thin lithosphere (e.g. Barletta et al., 2018), making the ice there sensitive to solid Earth and sea-level feedbacks. In the ASE, the Pine Island and Thwaites glaciers together contributed 95 Gt yr^{-1} of the $159 \pm 8 \text{ Gt yr}^{-1}$ total WAIS mass flux in 2017 (Rignot et al., 2019), with studies estimating that collapse of Thwaites Glacier is already underway (Joughin et al., 2014). Accurate GIA model predictions are critical to assess rates of future ice-sheet retreat and associated sea-level changes making it an ideal location to study the effects of grid resolution on modelled GIA. To represent the radially and laterally

variable Earth rheology in this region, we use a viscoelastic Earth rheology and a range of 3-D viscosity structure models in Antarctica derived from seismic tomography (An et al., 2015a; Heeszel et al., 2016; Lloyd et al., 2020). We adopt a range of 3-D Earth model grids with surface resolutions from 1.9 to 15 km and compare results to first assess the resolution required to capture the elastic deformation associated with ice loss. We then repeat these experiments with viscoelastic effects and compare results to the elastic calculations to assess the contribution of viscous effects to modern and future sea level, as well as the model resolution required to capture these effects. In the sections that follow, we describe the adopted 3-D GIA model, computational grids, Earth rheological models, and adopted modern and future ice loss scenarios.

2.1 3-D GIA model

We perform all our simulations with a global, 3-D, finite-volume GIA model (Latychev et al., 2005) capable of regional grid refinement (Gomez et al., 2018). The model solves the sea-level equation (Kendall et al., 2005) with time-varying shorelines over a 3-D, spherical, tetrahedral grid defined globally from the surface to the core–mantle boundary (CMB), allowing us to resolve the laterally and radially varying Earth structure that is a strong feature in Antarctica. We also adopt this 3-D GIA model because it is capable of regional grid refinement to achieve regional resolution at sub-kilometre scale in regions of interest within a lower-resolution globe (Sect. 2.2). The model computes deformation of the solid Earth and gravitationally self-consistent changes in position of the sea surface equipotential in response to applied ice loading changes accounting for the effects of perturbation in the Earth’s rotation and solid surface assuming an elastically compressible Maxwell viscoelastic rheology. Note that this henceforth called “GIA model” may also equivalently be referred to as a “sea-level model” in some literature.

The GIA model requires two main inputs: a 3-D Earth model of viscoelastic rheological properties and a time series of ice thickness changes (where the location of grounded ice may be prescribed or computed within the model if the ice thickness data include floating ice). These components are described in the following sections. The model also requires global ice-free topography as an initial boundary condition, including the elevation of the bedrock beneath the applied ice load. Outside of Antarctica, etopo2 from NOAA (NOAA National Geophysical Data Centre, 2006) is used in all experiments with a realistic loading scenario, and the Antarctic bedrock elevation for each of the experiments is described below. Note that we adopt a standalone GIA model throughout this study with the purpose to inform the set-up of coupled ice-sheet–GIA modelling studies, but we do not model the feedback of GIA effects on ice-sheet dynamics explicitly. However, other studies (e.g. Gomez et al., 2015; Kachuck

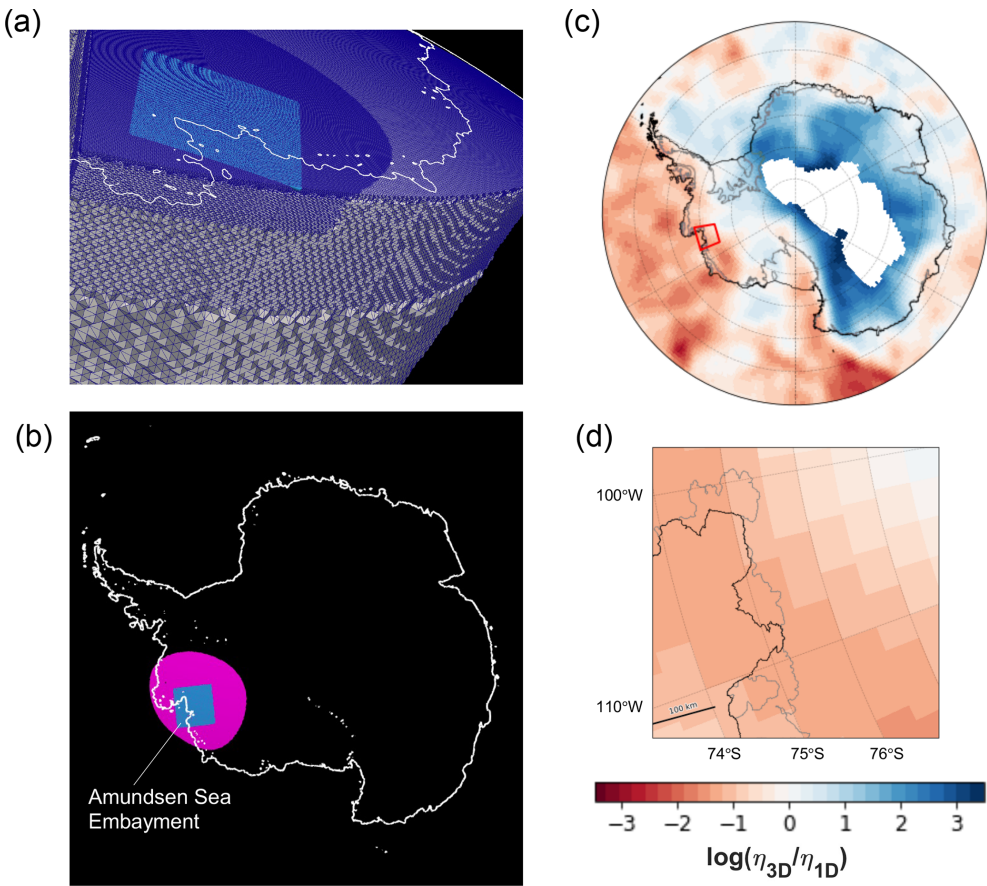


Figure 1. Grid and Earth model configuration. (a, b) Configuration of the tetrahedral grid in the finite-volume 3-D GIA model with regional refinement used for observational and modelled ice loading scenarios. Panel (a) shows a cross-sectional view of the regional refinement along ASE. Panel (b) indicates areas of grid refinement across Antarctica with a surface grid resolution of 7.5 km over all Antarctica in black, 3.75 km over a section of West Antarctica in magenta and 1.9 km in the ASE (light blue square). (c, d) Logarithmic viscosity perturbation map at a depth of 200 km for low-viscosity upper-mantle model EM1_L over (c) Antarctica and (d) our study region in the Amundsen Sea Embayment. Values are relative to a reference 1-D profile with upper-mantle viscosity of 1×10^{20} Pas and lower-mantle viscosity of 5×10^{21} Pas. The black line delimits the edge of the Antarctic ice shelf including the extent of marine-based ice, and the gray line shows the location of the grounding line from Bedmap2 (Fretwell et al., 2013). Transparent patch in (c) contains no data on mantle viscosity as the region contains lithosphere at 200 km depth.

et al., 2020) suggest that the scale of differences in solid Earth deformation and sea-level change simulated at different resolutions and adopting different Earth structure models here will be large enough to alter the timing and magnitude of grounding-line migration in a coupled modelling context.

2.2 Computational model grid: regional grid refinement

To compute GIA model predictions, we construct model grids of various surface resolutions (Fig. 1) with the regional grid refinement process detailed in the Supplement of Gomez et al. (2018). Grid refinement is achieved by incrementally bisecting grid edges over a selected 3-D region to achieve a desired resolution, as well as a final smoothing operation along the region boundary to ensure a well-behaved transi-

tion. We perform calculations on a base grid with a global surface resolution of 15 km, which consists of 20 million nodes and 70 radial layers between the core–mantle boundary and the Earth’s surface. The radial layers of the grid are defined to respect the unconformities in material properties of the radially varying (1-D) seismic reference model STW105 (Kustowski et al., 2008), with the shallowest layers at 12, 25 and 43 km depth. Eight regionally refined grids are constructed from this base grid: five for the idealised load sensitivity tests at 7.5, 3.75, 1.75, 1 and 0.5 km surface grid resolution over a minimum 0.3° radius region around the test load used in Sect. 3, and three for the more realistic calculations from observed modern and future model projected ice loss in Sect. 4 at 7.5, 3.75 and 1.9 km surface resolution in an incrementally smaller series of nested 3-D regions converging over the ASE (Fig. 1). Results in Sect. 4 are also

computed on the base grid of 15 km resolution. The highest-resolution 1.9 km grid over the ASE has ~ 29 million nodes, which takes ~ 65 CPU hours to run per time step on a high-performance computing cluster. As our study focusses on surface grid resolution, the 3-D grid refinement region is limited to the surface down to ~ 10 km depth where the grid is bisected incrementally both horizontally and vertically. Testing with deeper grid refinement during the experiment design process indicated that this was sufficient, and our results indicate that kilometre-scale model resolution is only needed at the surface to accurately capture the geometry of surface loading. For consistent comparison of results from various grid resolutions, all results from Sect. 4 are interpolated onto the same 221×221 node grid evenly spaced in distance spanning the study region.

2.3 Earth rheological model

The spatial pattern and amplitude of surface deformation in response to ice loading are dependent on the underlying Earth structure. For the idealised sensitivity tests in Sect. 3, we adopt a purely elastic Earth model with a 1-D elastic and density structure based on the Preliminary Reference Earth Model (Dziewonski and Anderson, 1981). In Sect. 4, we move to a set of realistic simulations using observed or modelled AIS ice loading, adopting 3-D viscoelastic Earth models with a range of viscosity structures constrained by seismic tomography (An et al., 2015a, b; Lloyd et al., 2020) and informed by global navigation satellite system (GNSS) inferences of local mantle structure. The elastic and density structures for these models are based on seismic reference model STW105 (Kustowski et al., 2008). Laterally varying lithospheric thickness (Fig. S1d in the Supplement) in all simulations is a composite of a regional lithospheric thickness model by An et al. (2015a) over Antarctica, as well as a global lithospheric thickness model by Conrad and Lithgow-Bertelloni (2006) everywhere else. Over Antarctica, lithospheric thickness is scaled to have an average of 96 km, resulting in a minimum of 40 km, as was done in Hay et al. (2017).

To establish lateral variations in mantle viscosity, we follow Latychev et al. (2005) and Austermann et al. (2013) by sequentially converting relative variations in isotropic shear wave velocity to density, temperature and eventually viscosity. The latter step admits a free scaling factor to scale temperature changes inside an exponential term. It follows that this free scaling factor can be tabulated under certain assumptions and appears to be slowly decreasing in magnitude with depth (see Sect. S2 in the Supplement for details). We chose to adopt a free scaling factor because, generally, a different scaling is required to account for the amplitude differences between global and regional seismic models when constructing a composite model.

To address the substantial uncertainty in Earth structure, we repeat our simulations with three different 3-D viscos-

ity models: EM1_L (Figs. 1c, d and S1), EM1_M and EM2. EM1_M and EM1_L adopt the latest high-resolution 25 km Antarctic seismic tomography model by Lloyd et al. (2020) (ANT-20) in the region south of 45° S and extending from the surface down to the transition zone, as well as S362ANI (Kustowski et al., 2008) for the rest of the globe. ANT-20 is provided on a 25 km grid at the surface, with the distance between the points decreasing with depth, and provided at depth slices in 5 km intervals from 0 to 800 km depth. S362ANI is a 3-D global anisotropic shear wave velocity model for the whole mantle, extending from 25 km depth to the core–mantle boundary defined at 2891 km depth, provided at a 2° lateral grid resolution at the surface. We note, however, that the spacing of the seismic model grid is distinct from the scale of the Earth structure variations captured by the model. While quantitatively assessing the latter remains an outstanding challenge in seismic tomography, we expect the resolution of the ANT-20 model to be $O(> 100$ km) in the upper mantle and coarser at greater depths and thus well represented by the GIA model grid. The two variations EM1_M and EM1_L were scaled to represent a moderate range of viscosities across Antarctica that match regional averages and a lower-viscosity endmember adjusted to match GPS-derived inferences of minimum viscosity beneath WAIS (Nield et al., 2014; Zhao et al., 2017; Barletta et al., 2018).

The viscosity variations in EM1_M are more moderate with scaling factors of 0.0263 K^{-1} for ANT-20 and 0.035 K^{-1} for S362ANI, both close to the value arising from Kaufmann et al. (2005) (see Sect. S2). These viscosity variations are superimposed on a 1-D viscosity profile of 5×10^{20} Pas in the upper mantle and 5×10^{21} Pas in the lower mantle typical in most GIA-based inferences of mantle viscosity (e.g. Mitrovica and Forte, 2004). As noted, the viscosity variations in EM1_L (Figs. 1c, d and S1) are of higher amplitude with lower viscosities under WAIS and the ASE. EM1_L adopts larger scaling factors of 0.033 K^{-1} for ANT-20 and 0.04 K^{-1} for S362ANI and an accompanying 1-D viscosity profile of 1×10^{20} Pas in the upper mantle, which is aligned with Lambeck et al.'s (2014) estimates of 1-D upper-mantle viscosity using far-field sea-level proxy records, and 5×10^{21} Pas in the lower mantle. The larger scaling factors applied in EM1_L were calibrated to best reflect the absolute upper-mantle viscosity estimates from GPS bedrock uplift rates at three locations: $\sim 6 \times 10^{17}$ to 2×10^{18} Pas at the northern Antarctic Peninsula (Nield et al., 2014), $\sim 2 \times 10^{19}$ to 2×10^{20} Pas at the Fleming Glacier in the central Antarctic Peninsula (Zhao et al., 2017), and $\sim 2.5 \times 10^{18}$ to 4×10^{19} Pas at the Amundsen Sea Embayment (Barletta et al., 2018). Figures 1c, d and S1 show the resulting low-viscosity Earth model structure (EM1_L), which has the lowest viscosity at Marie Byrd Land of $\sim 9 \times 10^{17}$ to 7×10^{18} Pas in the upper mantle.

Lastly, the EM2 model, also adopted in Hay et al. (2017), Gomez et al. (2018), and Powell et al. (2020), is a combina-

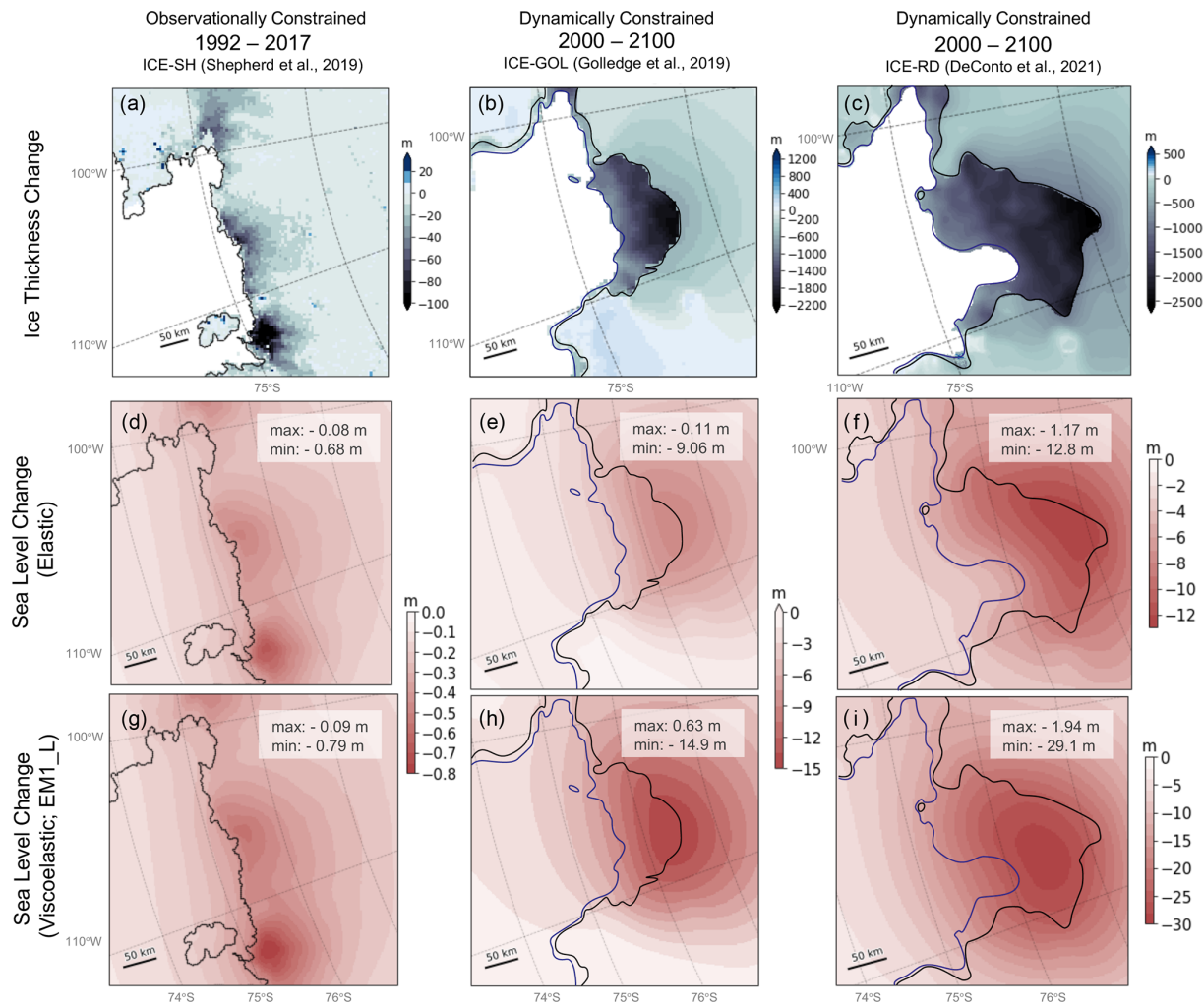


Figure 2. Ice loading scenarios and corresponding elastic sea-level predictions in the ASE. **(a–c)** Total ice thickness change in metres predicted from **(a)** 1992 to 2017 in the observation-based ICE-SH ice model (Shepherd et al., 2019) and from **(b)** 2000 to 2100 in the ICE-GOL (Golledge et al., 2019) and ICE-RD (DeConto et al., 2021) ice model projections. Panels **(d–f)** show the predicted sea-level change in metres with an elastic Earth model associated with the ice cover changes shown in **(a–c)**. Panels **(g–i)** are as in **(d–f)** but adopting 3-D viscoelastic Earth model EM1_L. All sea-level predictions were performed on a 1.9 km resolution grid. The black and blue lines indicate final and initial grounding lines, respectively, for each simulation. Each panel is annotated with the maximum and minimum value within the panel. Note that the colour bars change across each panel.

tion of three seismic models: S40RTS (Ritsema et al., 2011) globally, a model by An et al. (2015a) in East Antarctica and the Antarctic Peninsula, and the model by Heeszel et al. (2016) for West Antarctica. The full construction of EM2 is detailed in Hay et al. (2017).

2.4 Ice model and topography

We consider three ice melt scenarios with resolutions ranging from 1 to 5 km in the ASE. The total ice thickness change from start to end of each scenario is shown in Fig. 2a–c.

For observations of modern ice loss, we adopted a reconstruction we term ICE-SH from Shepherd et al. (2019) of surface elevation change (Δh) from 25 years (1992–2017)

of multi-mission satellite altimetry data resolved over a 5 km grid at 5-year intervals. We treat Δh as a proxy for ice thickness change (Carrivick et al., 2019) and apply the Bedmap2 (Fretwell et al., 2013) grounded ice mask and saturate ice thickness change to $> 20 \text{ m yr}^{-1}$ to control against spurious data points. Initial ice thickness and bedrock topography in Antarctica is given by Bedmap2. Observations of ice surface elevation changes in Antarctica are continuously improving in resolution and currently range from metre-scale resolution over short observational tracks (e.g. Studinger, 2014), to sub-kilometre to kilometre-scale resolution at the regional scale (e.g. Bamber et al., 2020), and to ~ 5 to 35 km resolution from radar and laser-satellite-altimetry-derived records over the whole Antarctic (e.g. Martin Espa  nol et al., 2016;

Schröder et al., 2019; Shepherd et al., 2019; Smith et al., 2020). ICE-SH was selected from the available observational datasets due to the 5 km resolution being the highest of its class of available satellite-altimetry-derived records providing decadal time span surface elevation change records covering the whole Antarctic.

For Antarctic evolution over the next century, we apply modelled ice thickness changes from two Antarctic-wide ice-sheet model projections named as follows: (1) ICE-GOL, which predicts AIS evolution under Representative Concentration Pathway (RCP) 8.5 and including meltwater feedbacks from 2000 to 2100 at 5 km resolution over 5-year intervals (Golledge et al., 2019), and (2) ICE-RD, which predicts AIS evolution from 1950 to 2100 at 10 km resolution over the whole AIS with a nested 1 km resolution simulation over ASE at annual resolution (“Extended Data” Fig. 5 from De-Conto et al., 2021). For ICE-RD, we ran simulations at yearly intervals from 1950 to 2100, but the interval from 1950 to 2000 is a period of ice model initialisation, and we therefore focus on the period between 2000 and 2100 in our results. We also take initial Antarctic bedrock topography from the ice models. Further information of each model can be found in the corresponding references. In selecting these scenarios, the goal is to provide a representative sample of spatially coherent ice-sheet retreat scenarios at high resolution from the literature rather than to capture all possible projected future ice loss scenarios.

When inputting a given ice load into the 3-D GIA model, the load mapper algorithm interpolates via a non-linear scheme, the equivalent load acting on each triangular area in the computational grid. Subsequently, an equivalent of 1/3 of the share of the load falling on each triangle grid area incident on the node is summed onto the loaded computational grid node. Within the computational grid triangle area, the load is assumed to be a linear function in triangular coordinates.

3 Idealised experiments: sensitivity of elastic uplift predictions to grid resolution

Our main goal in this analysis is to assess the relationship between grid resolution and GIA model predictions and to identify, for a given load dimension, the grid resolution required to accurately model the associated elastic Earth deformation component of the sea-level change. Realistic ice retreat has complex geometry, making it difficult to pinpoint the cause of inaccuracies due to resolution, which may be due to poor representation of the ice load or numerical errors in the representation of the response to Earth loading. To isolate the effect of changing grid resolution on sea-level predictions, we first perform a suite of idealised sensitivity tests using the GIA model described in Sect. 2.1 to make predictions of the instantaneous elastic deformation from the unloading of an isolated cylindrical ice load with differing surface grid

resolutions that are iteratively bisected from 7.5 km down to 0.5 km. We chose to perform the test with short-wavelength, spatially isolated ice-loading changes because these would be most poorly represented by a coarse grid compared to coherent ice loss over a broader area. Furthermore, these tests with idealised loads are less computationally costly and enable a systematic assessment reaching higher spatial resolution. In total, 85 simulations were run using 17 ice cylinders of height 100 m and radii ranging from 0.5 to 16 km (0.5, 1, 2, . . . , 15, 16) across five different grid surface resolutions: 0.5, 1, 1.75, 3.75 and 7.5 km.

The simulations are performed with the purely elastic 1-D Earth model (Sect. 2.3) and an idealised topography of 3800 m south of 24.5° S and –835 m everywhere else to reflect the 30 : 70 land to sea ratio on Earth (Fig. S2 in the Supplement). A radially symmetric ice sheet with steady-state Antarctic ice dome profile (Paterson, 1980) sits on top of this topography extending from the South Pole to 69° S, with a maximum height of 3500 m. We also consistently place the centre of the cylindrical load on an arbitrary model grid node in the ASE (76° S, 150° W). All results from Sect. 3 are plotted by interpolating onto the same 80 km box with 200 m resolution over the study region.

3.1 Idealised experiment results

Figure 3 summarises the error in the predicted elastic solid Earth deformation with varying load radius and grid resolution. Figure 3a shows the bedrock deformation along a transect from the centre of the load for ice cylinders with radii of 2, 5 and 10 km, with maximum bedrock uplift predicted on the finest 0.5 km grid of 48, 108 and 190 mm, respectively. Figure 3b indicates whether the grid over-represents (blue) or under-represents (red) the mass of the load within the model (i.e. where the “mass factor” is less or greater than 1). Errors in the solid Earth deformation predictions, reported relative to the result for the finest-resolution 0.5 km grid (yellow lines), are typically the largest at the load centre where they underestimate the magnitude of peak displacement. Although a coarser grid may either under- or over-estimate the mass of loading represented in our model (Fig. 3b), it will always dampen the magnitude (effective height) of the load by spreading the load area over a larger grid region. For example, a 5 km radius load will be represented by three grid nodes on a 7.5 km grid, resulting in an overestimated 11.25 km radius loading footprint. For certain radius and grid combinations, the wider load footprint on a coarser grid leads to another zone of peak error occurring outside the grounded load edge (e.g. compare dashed black line to yellow line in Fig. 3a). Even further from the load, the magnitude of deformation decreases, and the results from various grid resolutions begin to converge.

These sensitivity test results highlight that the accuracy of predictions depends on the placement of the edge of the load relative to grid nodes and find that the load will be best cap-

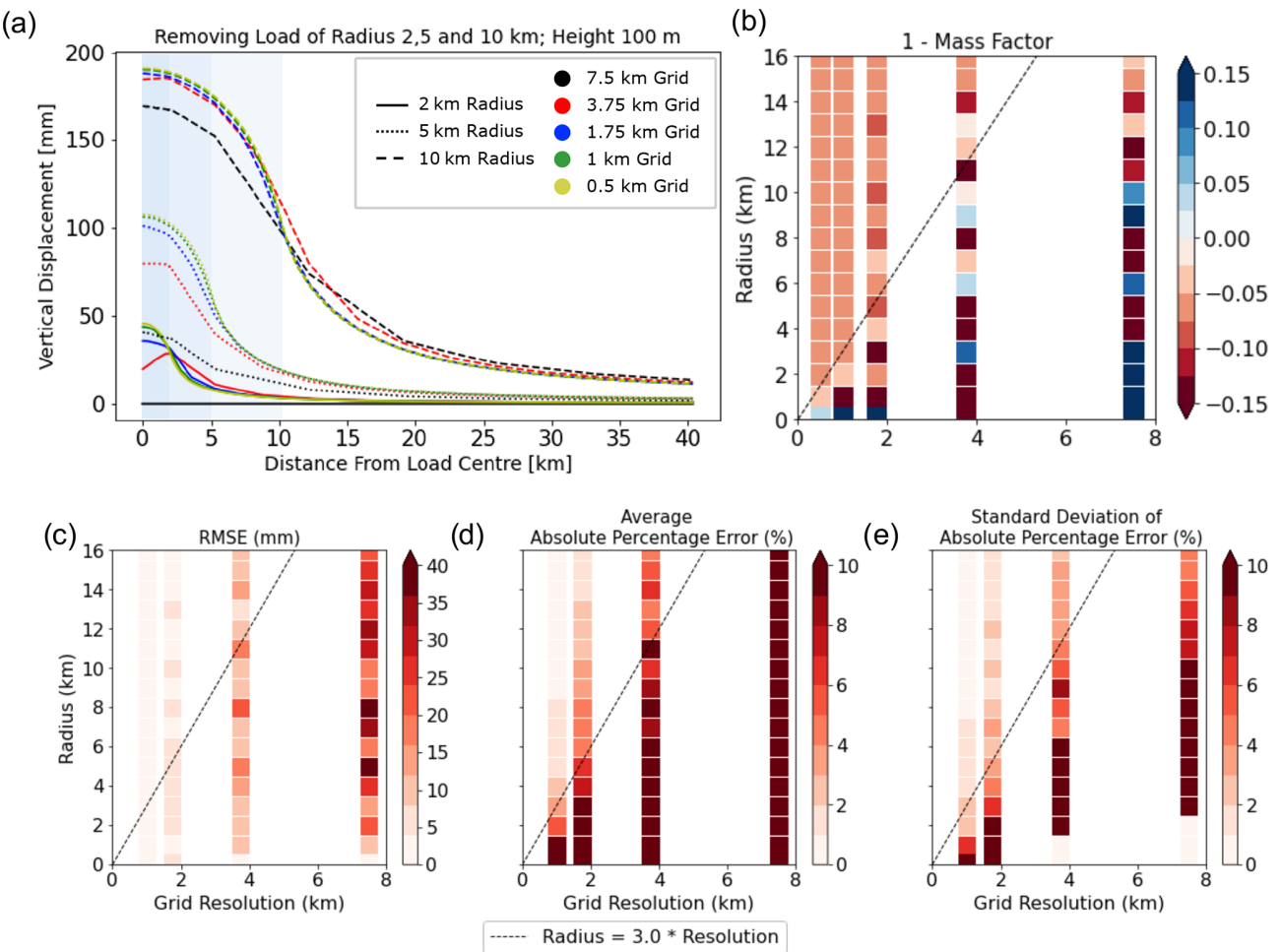


Figure 3. Idealised sensitivity experiment of the effect of surface grid resolution on GIA model calculations with elastic bedrock deformation due to instantaneous removal of cylindrical ice loads. Cylinders are all of unit height 100 m and radius from 0.5 to 16 km. Five grid resolutions applied within an area of minimum 40 km width were tested: 0.5, 1, 1.75, 3.75 and 7.5 km (Fig. S1). (a) Transect of bedrock deformation for removal of ice cylinders with unit height and radii of 2 km (solid lines), 5 km (dotted) and 10 km (dashed lines). (b) Results of a suite of simulations adopting ranges of ice cylinder radii and grid resolutions. (b) Colours indicate 1 minus the mass factor ($1 - \text{mass factor}$), in which the mass factor is the ratio of the theoretical mass of the load and the mass of the load represented on the given model grid; 0 represents a scenario in which the model grid perfectly represents the mass of the idealised load, whilst positive (blue) and negative (red) values indicate the load mass is over- and under-represented by model grid resolution, respectively. (c) Root mean square error across the suite of simulations (mm). (d) Average absolute percentage error (%). (e) Standard deviation of the absolute percentage error (%) of the given test from the finest 0.5 km resolution model result. Errors displayed on (c–e) are calculated within 2 km of the loaded region. Dashed black lines represent the 1 : 3 ratio between the surface grid resolution and idealised load cylinder radius, whereby average absolute percentage error becomes $< 7 \pm 3 (\sigma) \%$ for all scenarios. In panels (b–e) the colour bars are saturated according to the arrows on the respective colour bars.

tured if its edge lies sufficiently close to a grid node (e.g. in Fig. 3b the 1.75 km grid more closely captures the mass of a 2 km radius load than the 3 km radius load). Finally, the grid is unable to resolve the load when the grid resolution is more than approximately 3 times the radius of the load. This is illustrated, for example, in the solid black line in Fig. 3a, where unloading a 2 km radius load on a 7.5 km grid resulted in no deformation, whereas a 3 km radius load is captured with a 7.5 km grid.

To quantify grid-related error, we calculate the difference between a given simulation and the corresponding simulation with the finest (0.5 km) resolution. We plot the root mean square error (RMSE; Fig. 3c) as an absolute measure of error and the average and standard deviation of the absolute percentage error (Fig. 3d and e) as a relative measure of error beneath and within 2 km of the loaded region. Figure 3c shows that the magnitude of RMSE remains relatively constant. This RMSE remained between ~ 10 and 20 mm for a 3.75 km grid and ~ 20 and 40 mm for a 7.5 km grid, for ex-

ample. As the load radius increases, the magnitude of deformation increases as well. However, the error due to grid resolution becomes less significant relative to the total deformation (i.e. the percentage error in Fig. 3d and e decreases).

While the dependence of grid performance on load position relative to grid nodes complicates matters, in order to arrive at an approximate relationship between grid resolution and load size, we assume a linear relationship between the two, which allows us to estimate, for this GIA model, a threshold beyond which grid-related error becomes sufficiently low to no longer merit a further refinement in grid resolution (Fig. 3d and e). For example, in the cross-sectional view of deformation in Fig. 3a, the 10 km radius load deformation is equally well represented by grid resolutions between 0.5 and 1.75 km. Considering the average absolute percentage error (Fig. 3d and e), we found that a 1 : 3 ratio (represented visually on Fig. 3b–e in the form of a dashed black line) between grid resolution and load radius (1 : 6 ratio between grid resolution and load diameter) brings the error to $< 7 \pm 3\%$ (where 3 % represents 1 standard deviation of the absolute percentage error calculated within 2 km of the load region). Furthermore, the mass of the load is accurately captured with no more than $\sim 7.5\%$ error with this 1 : 3 ratio (Fig. 3b).

The results from this analysis of spatially isolated cylindrical loads provide a rough estimate of the magnitude of error one can expect from a given model resolution and loading scenario and can serve as a guide for selecting the appropriate grid resolution for a given problem. For example, for an input load with significant isolated locations of ice loss ~ 3 km in radius (or a ~ 6 km in diameter), a grid resolution of 1 km should be adopted. However, these idealised cylindrical load experiments are unlikely to capture the sensitivity of deformation and sea-level predictions to grid resolution when realistic ice loss geometries are adopted. Such geometries are rarely characterised by spatially localised loads. Furthermore, these experiments capture only elastic deformation and neglect viscous effects, which can be significant on short timescales in low-viscosity zones of the West Antarctic. In the following sections we explore how the dependence on grid resolution of GIA model predictions identified here changes when more realistic ice loss geometries and a 3-D viscoelastic Earth structure are adopted.

4 Results with realistic modern and future ice loss in the Amundsen Sea

In this section, we consider the importance of grid resolution error for more realistic, spatially coherent modern and future ice loss scenarios. We begin with a consideration of the influence of grid resolution on predicted sea-level change in simulations adopting a purely elastic Earth model in Sect. 4.1. Following this, we adopt 3-D viscoelastic Earth models to consider the contribution to sea-level change from viscous

deformation. Throughout Sect. 4, grid resolution error is defined as departures of predicted sea-level changes from the finest-resolution 1.9 km grid resolution result.

4.1 Influence of grid resolution on sea-level predictions with elastic deformation

Figure 2d–f show predicted sea-level change in the Amundsen Sea Embayment of West Antarctica adopting an elastic Earth model for three different ice retreat scenarios performed at a grid resolution of 1.9 km: one observationally constrained from 25 years of satellite altimetry data from 1992 to 2017 (ICE-SH; Fig. 2a), and two projected from dynamic ice-sheet models for the coming century (ICE-GOL and ICE-RD; Fig. 2b and c). Sea-level fall is predicted in the entire study region in all scenarios associated with the combination of sea surface subsidence and elastic bedrock uplift due to ice loss – the latter being the dominant signal. Earth rotational effects are included in the predictions but are negligible compared to the other effects in the vicinity of the ice loss. For the modern ice loss, the maximum sea-level fall from 1992 to 2017 reaches 0.68 m (Fig. 2d), while for future ice loss projections, the sea-level fall reaches up to 9.06 m and up to 12.8 m from 2000 to 2100 for ICE-GOL and ICE-RD, respectively. Note that in addition to the signal coming from local ice loss in the ASE, ice outside this region of interest also contributes a broad signal of smaller magnitude (see Sect. S1 in the Supplement).

To explore the resolution dependence of sea-level predictions that adopt an elastic Earth model, we repeat the calculations in Fig. 2d–f with a surface grid resolution ranging between 1.9 and 15 km. Figure 4a–i show the difference between results for simulations performed at 1.9 km grid resolution relative to coarser resolutions. The coarser grid simulations tend to underestimate the magnitude of ice unloading and associated sea-level fall in most of the domain (red regions in Fig. 4).

The highest grid resolution error occurs at the periphery of the load within a few kilometres of the final grounding-line position rather than at the location of maximum deformation (compare Fig. 4 to Fig. 2). This suggests that high resolution is necessary for better representation of the load at the grounding line rather than for representation of the smoother response of the solid Earth – a finding consistent with the idealised experiments discussed in Sect. 3 (see Fig. 3b). For example, for the ICE-GOL ice loss scenario, the greatest difference between 1.9 and 15 km grid simulation ranges occurs along the entire final grounding line (Fig. 4b), but the maximum sea-level fall of over 9 m occurs only on a concentrated region ~ 2 km away from the grounding line (Fig. 2e).

The error decreases with increasing resolution, with minimal differences between the 1.9 and 3.75 km grid resolutions. The maximum absolute error in the case of a 15 km grid (i.e. the maximum difference between the 15 and 1.9 km resolution cases) is 44 cm at 2100 in ICE-RD (Fig. 4c), 45 cm

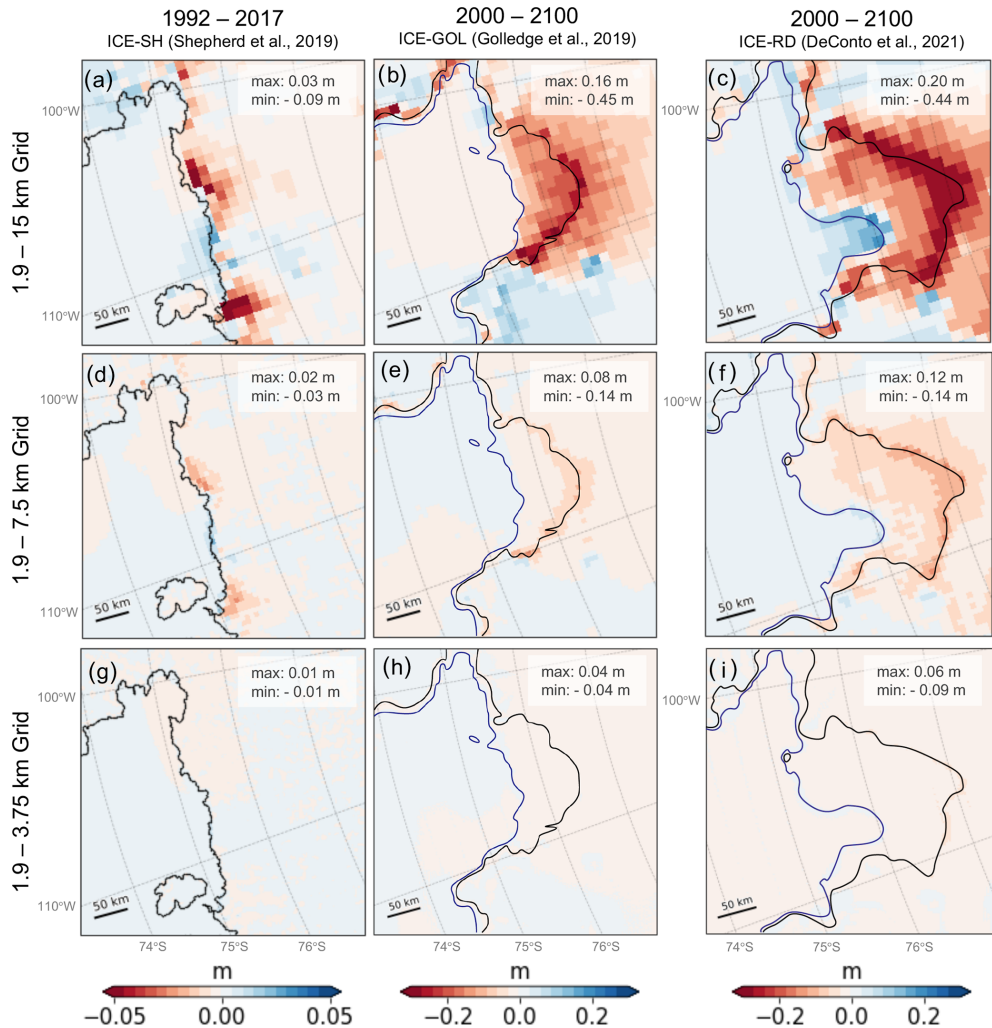


Figure 4. Influence of grid resolution on elastic sea-level predictions in ASE. Difference in predicted sea-level change in metres between (a–c) 1.9 and 15 km, (d–f) 1.9 and 7.5 km, and (g–i) 1.9 and 3.75 km resolution GIA model simulations with a purely elastic Earth model across the times indicated at the top of the column for the ice loading scenarios (from left to right) ICE-SH, ICE-GOL and ICE-RD. For each ice retreat scenario there is a different colour bar since the magnitude of error due to grid resolution differs. In some panels, the colour bar is saturated. The black and blue lines indicate final and initial grounding lines, respectively, for each simulation, and each panel is annotated with the maximum and minimum values within the panel.

at 2100 in ICE-GOL (Fig. 4b) and 8.7 cm after 25 years of modern melt in ICE-SH (Fig. 4a). That is 3.4 %, 5.0 % and 12.8 % of the peak elastic sea-level fall predicted at that time for each respective scenario. The errors are approximately an order of magnitude smaller when a grid resolution of 3.75 km is adopted: 9 cm for ICE-RD, 4 cm for ICE-GOL and 0.7 cm for ICE-SH or 0.7 %, 0.5 % and 1.0 % of the peak elastic sea-level fall, respectively.

Since maximum grid resolution error is concentrated along the grounding line for elastic simulations, in Fig. 5 we explore how the error evolves during the ICE-RD simulation along a 10 km region bounding the grounding line. The error increases in absolute magnitude with increasing ice loss (“Error” in Fig. 5), but the relative error decreases

across the same simulations (“Percentage Error” in Fig. 5). In the case of 15/7.5/3.75 km grid resolutions, the peak error is $\sim 10/5/1$ cm after 25 years in the simulations and $\sim 50/15/5$ cm after 150 years (whiskers in Fig. 5a top row). In contrast, the percentage error peaks at 20/6/1.5 % of the signal at 25 years and drops to $< 5/2/0.3$ % after 150 years (Fig. 5). This decrease in percentage error with time reflects that the ice geometry changes become broader in wavelength and can therefore be resolved by a coarser grid compared to the more spatially isolated changes occurring earlier in the simulation. Given the resolution in modelled and observed ice loss and bedrock elevation in Antarctica (e.g. Morlighem et al., 2020), we suggest that for most applica-

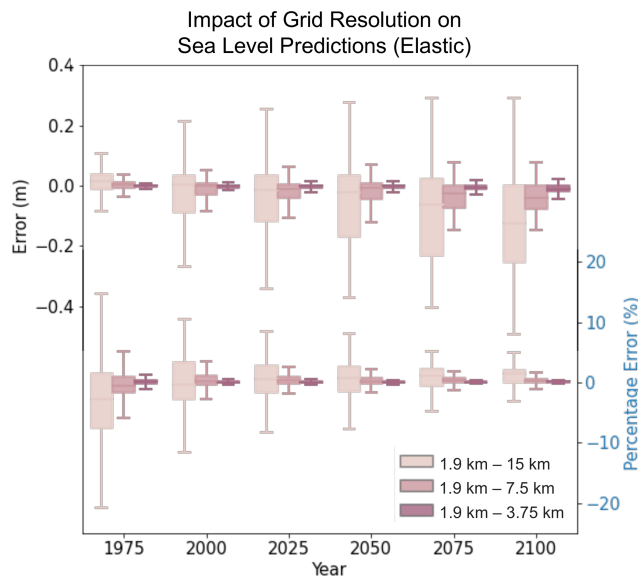


Figure 5. Evolution of error in elastic sea-level predictions due to grid resolution from 1950 to 2100 with the 1 km input resolution ICE-RD ice model. Box–whisker plots of the error and percent error (see methods) calculated from the difference in predicted sea-level changes from the start of the simulation to the indicated time within 10 km of the grounding line at that time between a simulation with 1.9 km resolution and simulations adopting 15 km (light pink), 7.5 km (medium pink) and 3.75 km (dark pink) grid resolutions. The box represents (from bottom to top) the 25th percentile, median and 75th percentile of the distribution, whilst the whiskers represent the “minimum” (25th percentile minus 1.5 times the interquartile range) and “maximum” (75th percentile plus 1.5 times the interquartile range). Error (m) is the difference between sea-level predictions from the higher–lower resolution simulation. Percentage error (%) is calculated as $100 \times (\text{SL}_{1.9\text{ km}} - \text{SL}_{\text{lowres}})/\text{SL}_{1.9\text{ km}}$ for each grid point.

tions, errors of less than 5 % can be achieved with a 7.5 km grid and errors of less than 2 % with a 3.75 km grid.

4.2 Contribution of viscous Earth deformation to sea-level predictions

So far we have focussed on the resolution dependence of the contribution to sea-level change from elastic Earth deformation as this has been a focus of recent literature (Larour et al., 2019). However, the Antarctic Ice Sheet is underlain by a strongly laterally varying viscosity structure, and the Amundsen Sea region in particular is underlain by a low-viscosity zone and thinned lithosphere (e.g. Barletta et al., 2018; Lloyd et al., 2020). Viscous deformation associated with ongoing ice loss is neglected in Larour et al. (2019) but is expected to be significant on decadal to centennial timescales in this region. In Fig. 2g–i the calculations of sea-level change associated with the three ice loss scenarios shown in Fig. 2d–f are repeated with the 3-D viscoelastic Earth model EM1_L described earlier. As with the elastic

case, sea level falls beneath regions that experience ice loss in all three cases, but the magnitude of the sea-level fall is significantly larger than predictions based on an elastic Earth model (compare Fig. 2g–i to Fig. 2d–f). In particular, peak sea-level fall in this case reaches -0.79 m over 25 years in the ICE-SH ice loss scenario and -14.9 and -29.1 m from 2000 to 2100 for ice loss scenarios ICE-GOL and ICE-RD, respectively. The latter (Fig. 2i) is more than double the sea-level fall calculated with the elastic Earth model (Fig. 2f).

Figure 6a–c show the contribution of viscous Earth deformation to the sea-level predictions, calculated by taking the difference between the full viscoelastic calculation shown in Fig. 2g–i and the calculation with an elastic Earth model shown in Fig. 2d–f. Over the 25-year modern ice loss scenario (Fig. 6a), viscous effects contribute up to 12 cm or 15 % of the peak viscoelastic prediction. In the future projections, within 100 years, the viscous contribution reaches up to 6.15 m of sea-level fall, or 41 % of the peak viscoelastic signal in predictions based on ICE-GOL, and up to 17.7 m of fall, or 61 % of the peak viscoelastic signal for ICE-RD, making viscous effects the dominant contributor over elastic effects in this latter case. For the future projections, compared with the elastic signal (Fig. 3e and f), the zones of maximum viscous uplift and sea-level fall (i.e. zones of intense red in Fig. 6b and c) are centred farther out beneath regions that experienced ice mass loss sooner in the simulation and have had more time for viscous deformation to occur (Fig. 6a–c), but as we highlight below, substantial viscous deformation still occurs along the current grounding line in the simulation. This is less evident in the modern ice loss because migration of the location of maximum ice mass loss is minimal. Faint blue areas further from the region of ice retreat in Fig. 6b indicate a sea-level rise due to peripheral bulge subsidence, a viscous process that results from the return flow of mantle material assuming viscous incompressibility.

4.3 Influence of resolution on sea-level predictions with viscoelastic deformation

In Fig. 7, we repeat the assessment of grid resolution error in Fig. 4 but with a viscoelastic rheology based on the 3-D Earth model EM1_L. With the inclusion of viscous behaviour, the magnitude of the grid resolution error is similar to the elastic case (compare the range of errors in Figs. 7 and 4), but the spatial pattern of the error becomes more complex. The maximum error is no longer solely concentrated along the current grounding line since the solid Earth continues to respond viscously to the poorly resolved loading changes along previous locations of the grounding line. This is particularly evident in the ICE-RD simulations where the grounding line retreats across a large area. In this case, the grid resolution error over the region of past ice loss and grounding-line migration is equal to or larger than the error along the active grounding line (Fig. 7b and c). The error increases during the simulation as viscous deformation builds and suggests

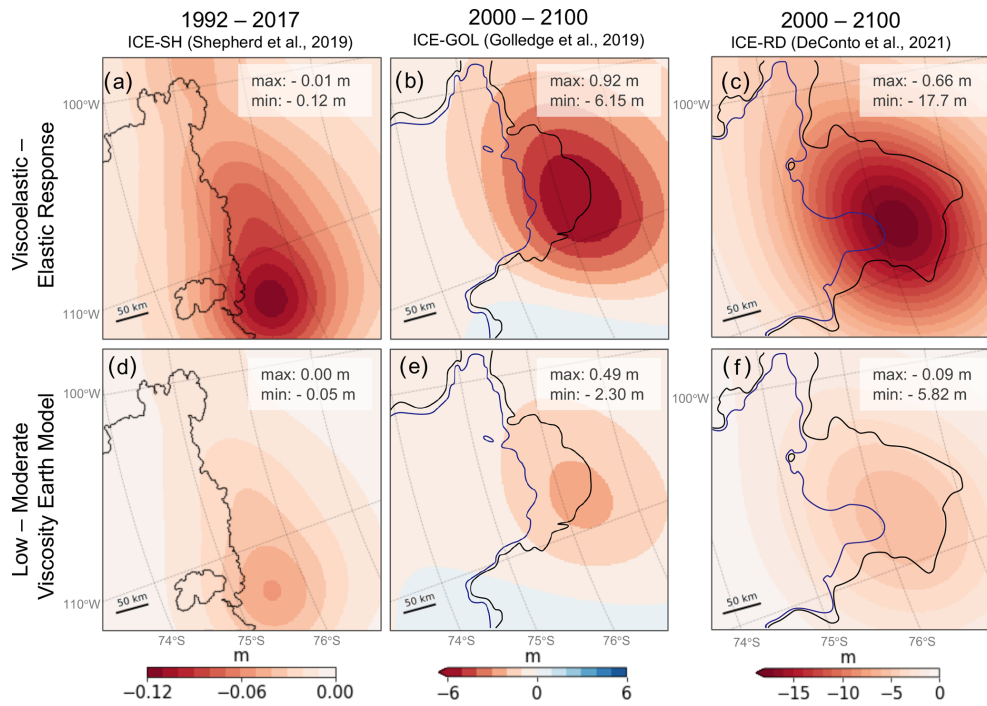


Figure 6. Influence of incorporating viscous behaviour and uncertainty in viscoelastic Earth structure on sea-level predictions. Panels (a–c) show the difference in sea-level change predicted from simulations adopting the 3-D viscoelastic Earth model EM1_L and an elastic Earth model. Panels (d–f) show the difference in sea-level change predicted from simulations adopting two different 3-D viscoelastic Earth models, EM1_L and EM1_M. Note the difference in scale. Time frames and ice models are as indicated at the top of the columns. In each panel, the black and blue lines indicate final and initial grounding lines, respectively, for each simulation and are annotated with the maximum and minimum data value within the panel. All simulations adopt a 1.9 km grid resolution.

it also has a dependence on the 3-D viscosity structure due to both lateral variation captured and the impact of a lower-than-average viscosity upper mantle in the WAIS, which we explore briefly in Sect. 4.3.

Note that in the blue region of Fig. 7c, the sign of the error is not the same as in Fig. 7f because ice retreat is not continuous within this particular region in ICE-RD. Specifically, between the years ~ 2020 and 2050 in ICE-RD, the grounding line in this blue region stays relatively fixed, experiencing multiple episodes of localised ice retreat and re-advance (unloading and loading). Situations of re-advance tend to occur at lateral scales < 15 km such that these sub-grid scale movements were not adequately captured with a coarser 15 km grid.

4.4 Earth model uncertainty

To investigate the influence of uncertainty in prescribed mantle viscosity structure, we compare simulations adopting five different Earth model configurations: a globally averaged 1-D viscoelastic Earth model, as used in EM1_M described in Sect. 2.3, a best fit 1-D viscoelastic Earth model for the WAIS described further in Sect. 4.5, and three 3-D mantle viscosity configurations derived from seismic tomography models (EM1_L, EM1_M and EM2; see Sect. 2.3). Figure 6d–f

show the difference in sea level predicted using the EM1_L and EM1_M models, which are based on the same underlying 3-D seismic velocity models but with different viscosity scaling factors and 1-D viscosity profiles. EM1_L (shown in Figs. 6a–c and 2g–i) has the lowest-viscosity upper mantle beneath the ASE. Red regions in Fig. 6d–f indicate locations of higher predicted sea-level fall due to lower-mantle viscosity and a shorter timescale of viscous response in EM1_L. Differences reach up to 5 cm after 25 years with ICE-SH and up to 2.3 and 5.8 m between 2000 and 2100 for ice loss scenarios ICE-GOL and ICE-RD, respectively. The simulation with EM2, a 3-D mantle viscosity model built from a different seismic tomography dataset, produced deformation with magnitudes intermediate to the simulations with EM1_L and EM1_M. We note that the rheology for this area is uncertain, and our experiments do not comprehensively capture the full range of this uncertainty (see Whitehouse et al., 2019, for a more detailed discussion).

4.5 Time evolution of influence of grid resolution and viscous effects

To compare the relative contributions of grid resolution and Earth model differences over time, we extract predicted sea-level time series from all simulations with the ICE-RD ice

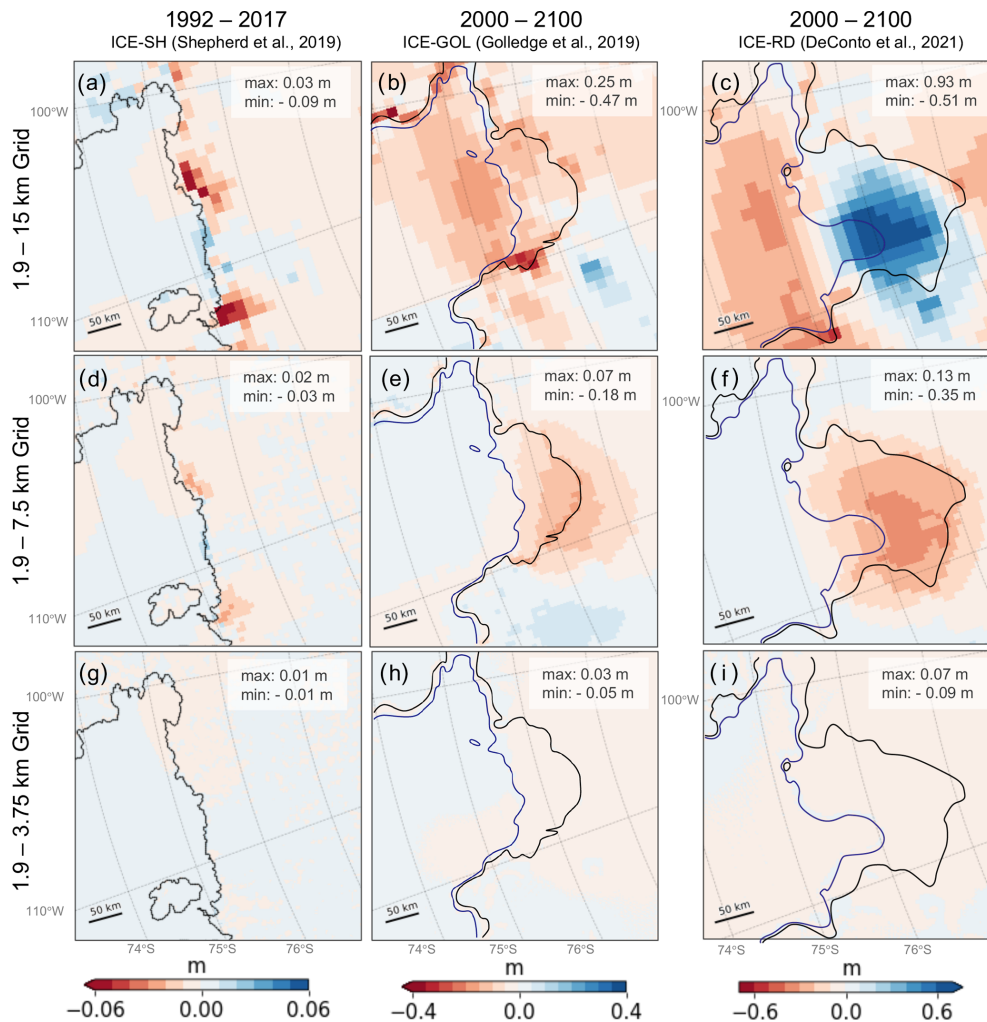


Figure 7. Influence of grid resolution on viscoelastic sea-level predictions in ASE. As in Fig. 4 but adopting the 3-D viscoelastic Earth model EM1_L.

loading scenario and elastic and viscoelastic Earth models at two locations in Fig. 8: (X) the region experiencing the largest viscous uplift by 2100 (blue star) and (Y) the location of maximum ice loss at the 2100 grounding line (red star). Note that the shaded grey region from 1950 to 2000 in Fig. 8b and c represents a time of hindcast spin-up to the year 2000 in the ice-sheet model simulation (see DeConto et al., 2021) rather than a realistic representation of the ice cover changes in this region over this time period. In the case of the globally averaged 1-D viscoelastic Earth model, the sea-level response is similar to the elastic case (Fig. 8, compare red and black lines) because the upper-mantle viscosity is set to 5×10^{20} Pa s, and thus a much longer timescale is required for viscous effects to become significant. In all cases, the differences between either the elastic or 1-D viscoelastic simulations and any of the viscoelastic simulations adopting 3-D Earth structure are substantially larger than the difference between the purely elastic and any 1-D viscoelastic simula-

tion. For example, the differences between simulations using EM1_L and the global average 1-D viscoelastic Earth model reach up to 16.5 and 12.7 m at the sites shown in Fig. 8b and c, respectively, by 2100.

To briefly explore the distinction between the impact on predictions of adding lateral variations in Earth structure and the impact of adopting a 1-D model with a lower than global average mantle viscosity profile representative of the structure underlying the WAIS, we ran an additional simulation adopting a 1-D viscoelastic Earth model for West Antarctica derived in Powell et al. (2022). This model has a viscosity of 3.2×10^{19} Pas in the shallow upper mantle, 1.3×10^{20} Pas in the deep upper mantle, 2.0×10^{20} Pas in the transition zone and 5×10^{21} Pas in the lower mantle. The predicted sea-level changes with the lower-viscosity WAIS 1-D Earth model shown by the purple lines in Fig. 8 lie closer to the 3-D Earth model results than the global average 1-D Earth model at sites X and Y. The degree to which the response

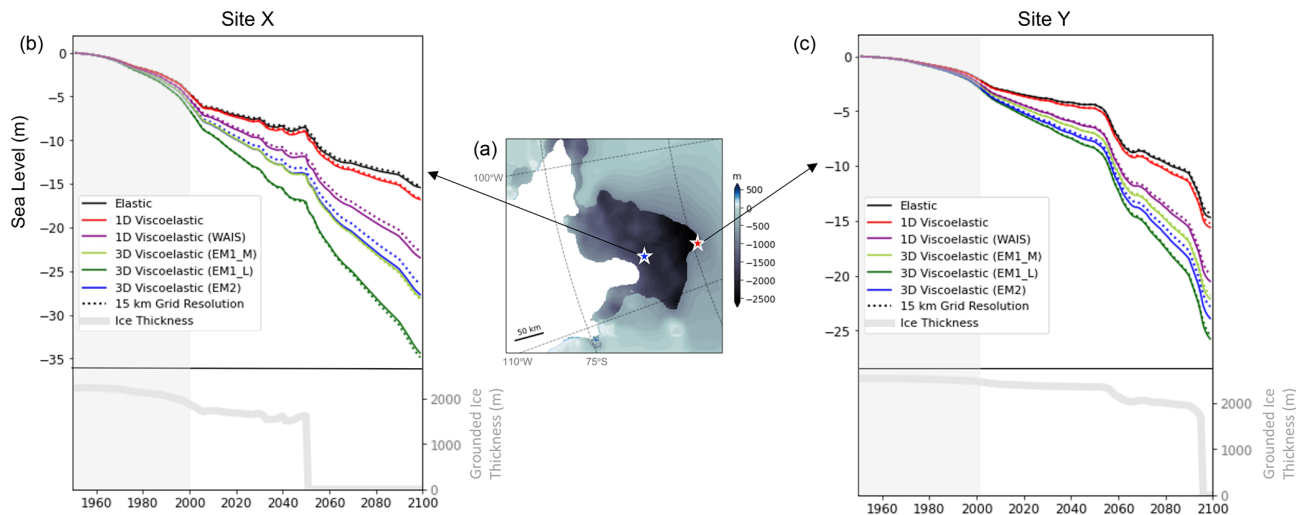


Figure 8. Evolution of site-specific sea level in simulations adopting a range of model resolutions and Earth models. (a) Ice thickness change from 2000 to 2100 predicted in the ICE-RD simulation. This panel is identical to Fig. 2c. (b) Coloured lines show predicted sea-level change, in metres, at Site X that experiences the maximum viscous uplift in the 1.9 km resolution simulation, shown by the blue star in panel (a). Each coloured line represents, respectively, the simulations with a purely elastic solid Earth response (black lines), viscoelastic solid Earth response based on a global average 1-D Earth model (red lines), a 1-D Earth model best-fit for the WAIS from Powell et al. (2022) (purple lines), a low-viscosity 3-D Earth model EM1_L (dark green lines), a moderate-viscosity 3-D Earth model EM1_M (light green lines) and 3-D viscosity Earth model EM2 (blue lines). Solid lines are for simulations performed at 1.9 km resolution, and dashed lines adopt a 15 km resolution. The thick gray line represents the evolution of grounded ice thickness at the respective sites. Panel (c) is as in panel (b) but for Site Y along the final grounding-line position at 2100 that experiences the greatest ice thickness change, labelled by the red star in panel (a).

of the laterally varying Earth structure in this region can be captured with a radially varying approximation is explored in more detail in Powell et al. (2022) and Blank et al. (2021).

Starting from 50 years into the simulation at the year 2000, the influence of grid resolution becomes smaller than the effect of adopting different Earth models (compare the differences between the dashed and solid lines to differences between different coloured lines in Fig. 8). Using the 1-D global average Earth model (Fig. 8 red lines), viscous effects start to emerge after 50 years and reach only 4 % of the peak signal by the end of the simulation. Nevertheless this signal is more significant than the error incurred by using 15 km versus 1.9 km grid resolution by 2040. With a 3-D Earth rheology and low viscosities beneath the ASE, viscous effects are pronounced within decades in the simulation (blue and green lines in Fig. 8) and become larger than the difference in predictions based on 15 and 1.9 km grid resolutions within 25–30 years and before substantial ice loss has occurred in the simulation.

Figure 9 provides a more detailed picture along the grounding line of the contributions to differences in predicted sea level described in the preceding sections. We consider the impact of each factor on the predicted sea-level signal at the end of the simulations, plotting the distribution of differences between simulations across all grid points within 10 km of the final grounding line. In interpreting Fig. 9, note once again that in viscoelastic simulations, the region of maximum grid resolution error does not necessarily occur near

the grounding line (e.g. Fig. 7c and f). To visualise the distribution, we plot a classic box–whisker diagram in which the edges of the boxes represent (from left to right) the 25th percentile, median and 75th percentile of the distribution, whilst the whiskers represent the “minimum” (25th percentile minus 1.5 times the interquartile range) and “maximum” (75th percentile plus 1.5 times the interquartile range), overlain by a density curve. A box–whisker plot was chosen to mitigate against the effect of outlier points, which we plot as hollow diamonds.

Note that the error due to grid resolution consistently has a unimodal distribution that peaks at $\sim 0\text{--}1\%$ near the grounding line across a range of durations from 25 years of ICE-SH to 100 and 150 years (starting from 1950) of ICE-RD. The hollow diamonds show that a significant number of points are statistical outliers, which is likely due to the fact that predicted sea-level change is low in magnitude in some regions along the grounding line that experience less ice loss, causing even a small magnitude of error to contribute a large percentage error. Inclusive of these outliers, the range of percent error due to a 15 km grid peaks at $\sim 20\%$ after 25 years in the ICE-SH simulation but decreases to less than $\pm 8\%$ by 100 years of the ICE-RD simulation as the magnitude of predicted sea-level fall becomes larger across the entire region, and the spread of outlier points diminishes. We conclude that the range denoted by the box–whisker plot likely provides a more accurate assessment of the error contributed by each factor in Fig. 9 in zones of active grounding-line mi-

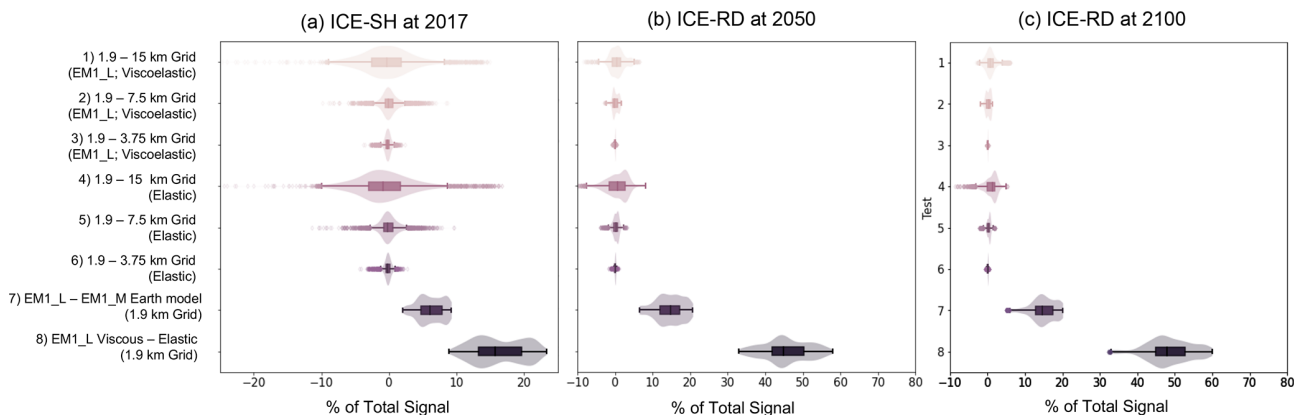


Figure 9. Comparison of factors contributing to differences in sea-level predictions in this study. Each distribution represents the influence of the specific factor across points within 10 km of the grounding line at the specified year of the simulation. For each factor, the “% total signal” is calculated as $(SL_A - SL_B)/SL_B \times 100\%$, where simulations A and B are described as per the labels on the y axis with the form “A – B” (e.g. for the distribution described as “1.9–15 km grid”, A refers to the 1.9 km grid simulation and B refers to the 15 km grid simulation). Distributions are presented for (a) ICE-SH ice model from 1992 to 2017, (b) ICE-RD ice model from 1950 to 2050, and (c) ICE-RD ice model from 1950 to 2100. Eight factors are compared in this figure, as labelled on the y axis. To visualise the distribution, we plot a classic box-whisker diagram overlain with a density curve. The edges of the box represent (from left to right) the 25th percentile, median and 75th percentile of the distribution, whilst the whiskers represent the “minimum” (25th percentile minus 1.5 times the interquartile range) and “maximum” (75th percentile plus 1.5 times the interquartile range). The diamonds outside the whiskers represent outliers.

gration. However, in the following paragraphs we continue to describe the range of errors inclusive of outlier points so as to not under-estimate the possible spread.

Our results indicate that the difference due to the choice of adopted Earth model equals and, in most cases, exceeds the size of the error due to grid resolution near the grounding line by the end of all our simulations. Over the 25-year modern observed ice loss scenario, the difference in predictions associated with Earth model configuration between results using EM1_L and EM1_M lies between $\sim 2\%$ and 10% within 10 km of the grounding line, which is within the range of error due to insufficient grid resolution in a viscoelastic simulation. The latter ranges from $\pm \sim 20\%$ with a 15 km grid, $\pm 6\%$ with a 7.5 km grid and $< 3\%$ with a 3.75 km grid at all grid points (range of the diamonds outside the shaded distributions in Fig. 9a, though noting the discussion above, the percent error is substantially smaller than these endmember values at most points). However, with more ice loss over longer timescales, the difference due to adopted Earth model far exceeds the grid resolution error (Fig. 9b and c).

If we look beyond the grounding line and consider the difference in predicted sea level between different adopted 3-D viscosity models in the entire study region (difference in results with EM1_L and EM1_M, plotted in Fig. 6d–f at 2100), the lower-viscosity model results in additional viscous deformation that is up to 10.2% , 21.4% and 20.9% of the total viscoelastic signal predicted with EM1_L after 25 years of ICE-SH, 100 years of ICE-RD and 150 years of ICE-RD, respectively. In all cases, the error due to neglecting viscous effects altogether far surpasses the error due to grid resolution with a 15 km grid (compare the bottom rows to top three rows

of Fig. 9b and c). For example, the lower-viscosity EM1_L model results in an additional viscous deformation that is up to 23.8% , 58.9% and 62.4% more than the predictions with an elastic Earth model near the grounding line after 25 years of ICE-SH, 100 years of ICE-RD and 150 years of ICE-RD, respectively.

5 Discussion

Our study provides an assessment of the model grid resolution needed to capture decadal- to centennial-scale Earth deformation and sea-level change in the vicinity of active ice loss. We targeted the ASE in West Antarctica as our study location as it is a region with ongoing and projected marine ice-sheet retreat and where low mantle viscosity and thin lithosphere result in a rapid and localised solid Earth response to ice loading. Whilst we focus on the ASE, since the resolution error is primarily associated with the representation of the ice load, our general conclusions on resolution requirements and results of the sensitivity experiments can be applied to any area of active, localised ice loading, for example, in other parts of Antarctica, in Greenland or in the vicinity of smaller glaciers. We adopted a 3-D GIA model to accurately capture the viscoelastic response at high resolution, including the complexity introduced by laterally varying Earth rheology in the region. Accurate assessments of solid Earth deformation from past and present ice evolution are important for constraining the negative sea-level–solid Earth feedback on ice-sheet retreat, as well as more accurate interpretation of geophysical observables. For the former, our study focusses

on the sensitivity of sea-level predictions along the ice-sheet grounding line where this feedback occurs in Fig. 9.

5.1 Influence of grid resolution

For our suite of simulations with elastic and viscoelastic Earth models, modern and 21st century ice loss scenarios, and surface grid resolution ranging between 15 and 1.9 km, we found that improvements in the accuracy of GIA model predictions with increasing grid resolution were limited, remaining within centimetres to decimetres at the grounding line. Furthermore, our results converged at higher resolutions, with errors from a 3.75 km grid resolution reaching at most 6 cm within 10 km of the grounding line in all simulations even when the input ice-sheet model results were available at 1 km resolution in the case of ICE-RD. The error introduced in assuming an elastic Earth model and neglecting viscous deformation in the ASE builds to an order of magnitude or larger than the grid resolution error within three to four decades and up to tens of metres by the end of the century. In addition, predictions adopting different 3-D Earth models that reflect the uncertainty in viscoelastic Earth structure in the region diverge by up to 1 m within 50 years and upwards of 2–3 m after 100 years in the simulation.

For coupled ice-sheet–GIA model applications, our results suggest that adopting high resolution in the ice-sheet model does not require a similarly high-resolution GIA model. In our simulations, a 3.75 km grid was sufficient to bring errors relative to the finest-resolution simulation to $< 2\%$ along the grounding line for all scenarios (Fig. 9). Furthermore, this percentage decreased over time in our simulations and would continue to decrease in multi-century and millennial simulations as the magnitude of viscous deformation and the scale of the ice loss continue to grow. While bedrock topography has smaller-scale features (Morlighem et al., 2020), our results suggest that the changes in topography will be less localised and may be computed at lower resolution relative to the ice-sheet dynamics and then interpolated and added to the initial topography on the higher-resolution ice-sheet model grid, as is done in, for example, Gomez et al. (2015) and DeConto et al. (2021).

Our results showing that the location of maximum error consistently lies along the grounding line for elastic Earth model simulations (Fig. 4a–c) suggest that the error due to coarse model resolution is predominantly a result of poor representation of surface ice cover changes rather than representation of the smoother response of the solid Earth. For the latter, we would expect the error to occur instead at the location of maximum sea-level response rather than in the vicinity of the edge of the load (compare differing spatial patterns in Fig. 2e and f to Fig. 4b and c). When the viscous response is incorporated, the time-evolving nature of viscous deformation leads to an additional peak in grid resolution error at locations predominantly downstream of the grounding line due to the inaccurate representation of past loading (Fig. 7).

This additional zone of error will not affect active ice-sheet grounding lines, though it may be important for the interpretation of modern records or lead to re-grounding of an ice shelf. Note that while the spatial pattern of the error differs, the magnitude of the error due to grid resolution was similar across both elastic and viscoelastic simulations.

Our findings on the size and source of resolution error are in contrast to recent work by Larour et al. (2019), who suggested that kilometre resolution was required to capture elastic deformation. This discrepancy may be due in part to Larour et al. (2019) considering only point loads in their idealised resolution experiment, while our conclusions are based on more realistic, spatially coherent ice loss scenarios. Differences may also arise due to the nature of the computational grid and processing of inputs (see Sect. 5.3) which should be explored in more detail in future GIA model inter-comparison efforts. Nevertheless, our predictions based on an elastic Earth model converge to theirs for more spatially broad loads.

One possible limitation in this study is that we do not reach sub-kilometre grid resolution in our GIA model, and our highest-resolution ice model is 1 km. In sensitivity tests with idealised loading scenarios in Sect. 3 we adopted a grid resolution as low as 0.5 km and found that a minimum 1 : 3 ratio between grid resolution and load radius was required for the error in predicted deformation to remain below $7 \pm 3(\sigma)\%$ along the grounding line, suggesting that a 3.75 km grid would be unable to capture a spatially isolated, < 1 km radius ice unloading event. That we did not see significant error at this resolution in the realistic simulations indicates that the ice cover changes are spatially coherent and there are no significant spatially isolated ice unloading events (i.e. no ice thickness changes occurring over only a few grid points) predicted in the 1 km resolution ICE-RD ice model simulation (Fig. 5).

To further investigate if short-wavelength, spatially isolated ice loss scenarios exist over Antarctica, we assessed the surface elevation change observables from 40 and 25 years of multi-mission satellite altimetry data by Schröder et al. (2019) and Shepherd et al. (2019), respectively, and 15 years of airborne laser altimetry from Operation IceBridge (OIB ATM L4; Studinger, 2014, updated 2018). While a more detailed investigation is merited, in our initial analysis of these datasets we noted that spatially isolated ice loss events have a lower magnitude and only persist over short timescales, and we found no evidence of high-magnitude, short-wavelength ice loss occurring with spatial scales < 5 km. Thus, we expect that spatially isolated ice unloading occurs rarely and will not have a significant impact on the overall accuracy of GIA model results in a given region. Nonetheless, with improving observational products and ice-sheet model resolutions, we expect to obtain regional-scale ice loading grids of sub-kilometre resolution that may warrant further study with a sub-kilometre GIA model grid (e.g. Durkin et al., 2020).

5.2 Influence of viscous deformation and Earth model uncertainty

Within decades in the ASE, viscous deformation is a significant contributor to the GIA signal (Hay et al., 2017; Barletta et al., 2018; Powell et al., 2020; Kachuck et al., 2020). The GIA response can be decomposed into the following: perturbation of the sea surface equipotential, elastic deformation and viscous deformation of the solid Earth surface. Previous studies have isolated and assessed the relative importance of each of these contributions on ice-sheet dynamics. Over decadal to centennial timescales, Larour et al. (2019) confirmed that purely elastic deformation was more significant than the sea surface perturbation on continental scales, while Kachuck et al. (2020) highlighted that viscous deformation can contribute dominantly. In this study, we have confirmed that viscous deformation effects are significant within decades, particularly in the low-viscosity region of the ASE where the viscous component of deformation can reach multi-metre scales by the end of the century. This body of work highlights the importance of incorporating viscous behaviour in GIA modelling applications in regions of low mantle viscosity.

Complicating efforts to accurately characterise viscous deformation is the uncertainty in Earth's viscosity structure. The timescale of viscous solid Earth deformation on ice-sheet dynamics is strongly dependent on the assumed Earth rheology. The global average mantle viscosity of $\sim 10^{21}$ Pa s (Forte and Mitrovica, 1996) corresponds to response times from centuries to millennia, whilst recent seismic (Lloyd et al., 2020) and GPS observations suggest an upper-mantle viscosity under the ASE as low as $\sim 10^{18}$ Pa s (Barletta et al., 2018). Rapid viscous uplift response was similarly identified in Kachuck et al. (2020), who created a 2-D GIA model of mantle viscoelastic deformation and found that sea-level fall associated with viscoelastic mantle deformation led to a 30 % reduction in modelled ice-sheet volume loss by 2150. Our study compares results generated with three 3-D Earth rheology models; EM1_M and EM2 have a comparable viscosity range, while EM1_L has the lowest viscosity values under the ASE. We find that uncertainties associated with Earth structure are significant and can contribute up to multiple metres of uncertainty in predicted sea level by the end of a 100-year simulation (Fig. 6). Furthermore, additional uncertainty arises from the model of viscoelastic behaviour. We adopt a viscous Maxwell rheology, but studies suggest that incorporating a short-term transient component of deformation may result in even faster viscous deformation (e.g. Pollitz, 2019).

Finally, we note that the required resolution of the GIA model grid will depend on the resolution of the seismic model used to construct the 3-D Earth structure model. Earth structure is currently resolved in seismic tomography models in Antarctica at length scales of $O(100\text{ km})$ or greater (Lloyd et al., 2020; Lucas et al., 2020), but as further improvements in the resolution of seismic tomography emerge,

variations in Earth properties at even shorter spatial scales may be revealed and need to be represented in GIA models. However, given the smooth nature of viscoelastic deformation and geoid changes, we expect that the wavelength of ice loading variations will remain the determining factor of surface GIA model grid resolution requirements.

5.3 On GIA model set-up

In choosing a method for representing a finer-resolution load grid onto a coarser GIA model grid, we found that it is important to consider how the model itself discretises the load and the input load interpolation schemes. Here, it is worth noting that our GIA model grid is a tetrahedral grid (triangular grid on surface), and these findings may not translate perfectly to other model grid compositions. Our GIA model grid consists of a uniform global tetrahedral grid that allows for regional patches of refined resolution (also uniform) but does not permit matching of model grid nodes to the input grid. For our experiments, by comparing the volumes of the input ice calculated on the input and GIA model grids, we found that the inbuilt Poisson interpolation scheme (Latychev et al., 2005) performed better in interpolating the finest-resolution load grid onto the model grid compared to other tested schemes, suggesting that an understanding of the method in which the load is mapped onto the model grid nodes is important. Additionally, we note that considerations such as the resolution of the input ice-sheet model and treatment of the ice cover outside the region of interest also have an influence on the final GIA model predictions (see Sect. S1) and should be explored further in future studies.

6 Conclusion

In this study, we present a comprehensive analysis of the influence of grid resolution on GIA model predictions in response to ice cover changes in the ASE over the modern satellite era and through the 21st century. We adopt a range of Earth models including models that capture lateral variations in Earth structure based on seismic tomography and GNSS analyses. These experiments showed that (1) the grid resolution error introduced through adopting a 15 km grid relative to a 1.9 km model grid remains within centimetres to decimetres (which can reach up to 20 % of the total signal along the grounding line) throughout our simulations; (2) the grid resolution error is the highest in the vicinity of the grounding line for purely elastic deformation cases, as well as along past and current grounding lines for viscoelastic Earth models, and is primarily associated with the representation of the surface load; and (3) results with grid refinement beyond 3.75 km converged in our simulations even when adopting a 1 km resolution input load, and this likely represents a conservative lower bound since the next coarser grid we considered was 7.5 km. The errors associated with the choice of grid reso-

lution will decrease with time for longer simulations as the extent and magnitude of ice loss and associated Earth deformation and sea-level change increase. A comparison of simulations adopting elastic and 3-D viscoelastic Earth models demonstrates that the contribution of viscous deformation can be up to tens of metres over the 21st century or $> 60\%$ of the total deformation signal. Furthermore, uncertainties in Earth properties can contribute up to several metres of error. This indicates the importance of considering viscous deformation when modelling GIA over decadal to centennial timescales in the ASE. In comparison, the error due to grid resolution is negligible, especially for grids of 3.75 km spacing and less.

To supplement these findings with realistic ice loading, we conducted a sensitivity test with cylindrical loads with radii from 16 to 0.5 km and grid resolutions from 7.5 to 0.5 km. These experiments indicated a minimum 1 : 3 ratio between the required grid resolution and the load radius (i.e. grid size should be $\leq 1/3$ of the load radius) to minimise model grid resolution error. However, no significant spatially isolated loads occur in our adopted observation- and model-based ice loss scenarios, and a preliminary examination of other ice observation and modelled products suggests that significant ice loss with < 5 km wavelength is rare in the ASE. These results, taken together, support the conclusion that kilometre-scale resolution in GIA modelling is generally not necessary. However, as higher-resolution sub-kilometre ice observational and dynamic ice model grid products are released, this guidance may need to be revisited.

Code and data availability. We have made all model output from the sensitivity tests and more realistic simulations available on a public repository at https://osf.io/2vmqh/?view_only=4d08e562720941688e0644b80781eeaa (last access: 21 January 2022; Gomez and Wan Xiu Wen, 2021). The 3-D GIA model adopted here has been used in numerous previous studies; questions regarding the model or requests for additional output can be discussed with the corresponding author and Konstantin Latychev, the developer of the code. Additional data related to this paper may be requested from the authors.

Supplement. The supplement related to this article is available online at: <https://doi.org/10.5194/tc-16-2203-2022-supplement>.

Author contributions. JXWW and NG developed the ideas and experiments in the study with input from KL and HH. KL contributed to designing the experimental set-up. JXWW performed the simulations and analysis. JXWW and NG wrote the original text, and all authors contributed to revisions.

Competing interests. The contact author has declared that neither they nor their co-authors have any competing interests.

Disclaimer. Publisher's note: Copernicus Publications remains neutral with regard to jurisdictional claims in published maps and institutional affiliations.

Acknowledgements. We thank the reviewers, Samuel Kachuck and Grace Nield, and editor, Pippa Whitehouse, for their insightful feedback that helped us to improve the manuscript. This study was carried out during the COVID-19 pandemic, with co-authors working fully online from three different time zones in Canada, Singapore and South Korea, and we would like to acknowledge the editorial team for their flexibility and understanding during these extenuating circumstances. We thank Andrew Lloyd for providing the high-resolution Antarctic seismic tomography model used in our simulations and Evelyn Powell for discussions on estimating best-fit 1-D Earth models for WAIS that informed our analysis.

Financial support. This research has been supported by the Natural Sciences and Engineering Research Council of Canada (grant no. RGPIN-2016-05159), the Canada Research Chairs (grant no. 241814) and the Canadian Foundation for Innovation.

Review statement. This paper was edited by Pippa Whitehouse and reviewed by Samuel Kachuck and Grace Nield.

References

- Adhikari, S., Ivins, E. R., and Larour, E.: ISSM-SESAW v1.0: mesh-based computation of gravitationally consistent sea-level and geodetic signatures caused by cryosphere and climate driven mass change, *Geosci. Model Dev.*, 9, 1087–1109, <https://doi.org/10.5194/gmd-9-1087-2016>, 2016.
- An, M., Wiens, D. A., Zhao, Y., Feng, M., Nyblade, A. A., Kanao, M., Li, Y., Maggi, A., and Lévéque, J. J.: S-velocity model and inferred Moho topography beneath the Antarctic Plate from Rayleigh waves, *J. Geophys. Res.-Sol. Ea.*, 120, 359–383, <https://doi.org/10.1002/2014JB011332>, 2015a.
- An, M., Wiens, D. A., Zhao, Y., Feng, M., Nyblade, A., Kanao, M., Li, Y., Maggi, A., and Lévéque, J. J.: Temperature, lithosphere–asthenosphere boundary, and heat flux beneath the Antarctic Plate inferred from seismic velocities, *J. Geophys. Res.-Sol. Ea.*, 120, 8720–8742, <https://doi.org/10.1002/2015JB011917>, 2015b.
- Austermann, J., Mitrovica, J. X., Latychev, K., and Milne, G. A.: Barbados-based estimate of ice volume at Last Glacial Maximum affected by subducted plate, *Nat. Geosci.*, 6, 553–557, <https://doi.org/10.1038/ngeo1859>, 2013.
- Bamber, J. L. and Dawson, G. J.: Complex evolving patterns of mass loss from Antarctica's largest glacier, *Nat. Geosci.*, 13, 127–131, <https://doi.org/10.1038/s41561-019-0527-z>, 2020.
- Barletta, V. R., Bevis, M., Smith, B. E., Wilson, T., Brown, A., Bordoni, A., Willis, M., Khan, S. A., Rovira-Navarro, M., Dalziel, I., Smalley, R., Jr., Kendrick, E., Konfal, S., Caccamise 2nd, D. J., Aster, R. C., Nyblade, A., and Wiens, D. A.: Observed rapid bedrock uplift in Amundsen Sea Embayment promotes ice-sheet stability, *Science*, 360, 1335–1339, <https://doi.org/10.1126/science.aa01447>, 2018.

Berger, S., Favier, L., Drews, R., Derwael, J.-J., and Pattyn, F.: The control of an uncharted pinning point on the flow of an Antarctic ice shelf, *J. Glaciol.*, 62, 37–45, <https://doi.org/10.1017/jog.2016.7>, 2016.

Blank, B., Barletta, V., Hu, H., Pappa, F., and van der Wal, W.: Effect of lateral and stress-dependent viscosity variations on GIA induced uplift rates in the Amundsen Sea Embayment, *Geochem. Geophys. Geosy.*, 22, e2021GC009807, <https://doi.org/10.1029/2021GC009807>, 2021.

Carrivick, J. L., Davies, B. J., James, W. H., McMillan, M., and Glasser, N. F.: A comparison of modelled ice thickness and volume across the entire Antarctic Peninsula region, *Geogr. Ann. A*, 101, 45–67, <https://doi.org/10.1080/04353676.2018.1539830>, 2019.

Conrad, C. P. and Lithgow-Bertelloni, C.: Influence of continental roots and asthenosphere on plate-mantle coupling, *Geophys. Res. Lett.*, 33, L05312, <https://doi.org/10.1029/2005GL025621>, 2006.

Cornford, S., Martin, D., Lee, V., Payne, A., and Ng, E.: Adaptive mesh refinement versus subgrid friction interpolation in simulations of Antarctic ice dynamics, *Ann. Glaciol.*, 57, 1–9, <https://doi.org/10.1017/aog.2016.13>, 2016.

Coulson, S., Lubeck, M., Mitrovica, J. X., Powell, E., Davis, J. L., and Hoggard, M. J.: The Global Fingerprint of Modern Ice-Mass Loss on 3-D Crustal Motion, *Geophys. Res. Lett.*, 48, e2021GL095477, <https://doi.org/10.1029/2021GL095477>, 2021.

de Boer, B., Stocchi, P., and van de Wal, R. S. W.: A fully coupled 3-D ice-sheet-sea-level model: algorithm and applications, *Geosci. Model Dev.*, 7, 2141–2156, <https://doi.org/10.5194/gmd-7-2141-2014>, 2014.

DeConto, R. M., Pollard, D., Alley, R. B., Velicogna, I., Gasson, E., Gomez, N., Sadai, S., Condron, A., Gilford, D. M., Ashe, E. L., Kopp, R. E., Li, D., and Dutton, A.: The Paris Climate Agreement and future sea-level rise from Antarctica, *Nature*, 593, 83–89, <https://doi.org/10.1038/s41586-021-03427-0>, 2021.

Durand, G., Gagliardini, O., Zwinger, T., Le Meur, E., and Hindmarsh, R. C.: Full Stokes modelling of marine ice sheets: influence of the grid size, *Ann. Glaciol.*, 50, 109–114, <https://doi.org/10.3189/172756409789624283>, 2009.

Durkin IV, W., Wilson, T. J., Hansen, J. S., Willis, M. and Bevis, M. G.: Reevaluating the Elastic Response to Ice Mass Change in Antarctica, in: AGU Fall Meeting Abstracts, 2020, G012–0023, 2020.

Dziewonski, A. M. and Anderson, D. L.: Preliminary reference Earth model, *Phys. Earth Planet. In.*, 25, 297–356, [https://doi.org/10.1016/0031-9201\(81\)90046-7](https://doi.org/10.1016/0031-9201(81)90046-7), 1981.

Favier, L., Gagliardini, O., Durand, G., and Zwinger, T.: A three-dimensional full Stokes model of the grounding line dynamics: effect of a pinning point beneath the ice shelf, *The Cryosphere*, 6, 101–112, <https://doi.org/10.5194/tc-6-101-2012>, 2012.

Forte, A. M. and Mitrovica, J. X.: New inferences of mantle viscosity from joint inversion of long-wavelength mantle convection and post-glacial rebound data, *Geophys. Res. Lett.*, 23, 1147–1150, <https://doi.org/10.1029/96GL00964>, 1996.

Fretwell, P., Pritchard, H. D., Vaughan, D. G., Bamber, J. L., Barraclough, N. E., Bell, R., Bianchi, C., Bingham, R. G., Blankenship, D. D., Casassa, G., Catania, G., Callens, D., Conway, H., Cook, A. J., Corr, H. F. J., Damaske, D., Damm, V., Ferraccioli, F., Forsberg, R., Fujita, S., Gim, Y., Gogineni, P., Griggs, J. A., Hindmarsh, R. C. A., Holmlund, P., Holt, J. W., Jacobel, R. W., Jenkins, A., Jokat, W., Jordan, T., King, E. C., Kohler, J., Krabill, W., Riger-Kusk, M., Langley, K. A., Leitchenkov, G., Leuschen, C., Luyendyk, B. P., Matsuoka, K., Mouginot, J., Nitsche, F. O., Nogi, Y., Nost, O. A., Popov, S. V., Rignot, E., Rippin, D. M., Rivera, A., Roberts, J., Ross, N., Siegert, M. J., Smith, A. M., Steinhage, D., Studinger, M., Sun, B., Tinto, B. K., Welch, B. C., Wilson, D., Young, D. A., Xiangbin, C., and Zirizzotti, A.: Bedmap2: improved ice bed, surface and thickness datasets for Antarctica, *The Cryosphere*, 7, 375–393, <https://doi.org/10.5194/tc-7-375-2013>, 2013.

Gladstone, R. M., Payne, A. J., and Cornford, S. L.: Resolution requirements for grounding-line modelling: sensitivity to basal drag and ice-shelf buttressing, *Ann. Glaciol.*, 53, 97–105, <https://doi.org/10.3189/2012AoG60A148>, 2012.

Golledge, N. R., Keller, E. D., Gomez, N., Naughten, K. A., Bernales, J., Trusel, L. D., and Edwards, T. L.: Global environmental consequences of twenty-first-century ice-sheet melt, *Nature*, 566, 65–72, <https://doi.org/10.1038/s41586-019-0889-9>, 2019.

Gomez, N. and Wan Xiu Wen, J.: Resolving GIA in response to modern and future ice loss at marine grounding lines in West Antarctica, OSFHome [data set], <https://osf.io/2vmqh/?view-only=4d08e562720941688e0644b80781eeaa> (last access: 21 January 2022), 2021.

Gomez, N., Mitrovica, J. X., Huybers, P., and Clark, P. U.: Sea level as a stabilizing factor for marine-ice-sheet grounding lines, *Nat. Geosci.*, 3, 850–853, <https://doi.org/10.1038/ngeo1012>, 2010.

Gomez, N., Pollard, D., and Mitrovica, J. X.: A 3-D coupled ice sheet-sea level model applied to Antarctica through the last 40 ky, *Earth Planet. Sc. Lett.*, 384, 88–99, <https://doi.org/10.1016/j.epsl.2013.09.042>, 2013.

Gomez, N., Pollard, D., and Holland, D.: Sea-level feedback lowers projections of future Antarctic Ice-Sheet mass loss, *Nat. Commun.*, 6, 8798, <https://doi.org/10.1038/ncomms9798>, 2015.

Gomez, N., Latychev, K., and Pollard, D.: A coupled ice sheet-sea level model incorporating 3D earth structure: variations in Antarctica during the last deglacial retreat, *J. Climate*, 31, 4041–4054, <https://doi.org/10.1175/JCLI-D-17-0352.1>, 2018.

Han, H. K., Gomez, N., and Wan, J. X. W.: Capturing the interactions between ice sheets, sea level and the solid Earth on a range of timescales: a new “time window” algorithm, *Geosci. Model Dev.*, 15, 1355–1373, <https://doi.org/10.5194/gmd-15-1355-2022>, 2022.

Hay, C. C., Lau, H. C., Gomez, N., Austermann, J., Powell, E., Mitrovica, J. X., Latychev, K., and Wiens, D. A.: Sea level fingerprints in a region of complex Earth structure: The case of WAIS, *J. Climate*, 30, 1881–1892, <https://doi.org/10.1175/JCLI-D-16-0388.1>, 2017.

Heeszel, D. S., Wiens, D. A., Anandakrishnan, S., Aster, R. C., Dalziel, I. W., Huerta, A. D., Nyblade, A. A., Wilson, T. J., and Winberry, J. P.: Upper mantle structure of central and West Antarctica from array analysis of Rayleigh wave phase velocities, *J. Geophys. Res.-Sol. Ea.*, 121, 1758–1775, <https://doi.org/10.1002/2015JB012616>, 2016.

Ivins, E. R. and Sammis, C. G.: On lateral viscosity contrast in the mantle and the rheology of low-frequency geodynamics, *Geophys. J. Int.*, 123, 305–322, <https://doi.org/10.1111/j.1365-246X.1995.tb06856.x>, 1995.

Joughin, I., Smith, B. E., and Medley, B.: Marine ice sheet collapse potentially under way for the Thwaites Glacier Basin, West Antarctica, *Science*, 344, 735–738, <https://doi.org/10.1126/science.1249055>, 2014.

Kachuck, S. B., Martin, D. F., Bassis, J. N., and Price, S. F.: Rapid viscoelastic deformation slows marine ice sheet instability at Pine Island Glacier, *Geophys. Res. Lett.*, 47, e2019GL086446, <https://doi.org/10.1029/2019GL086446>, 2020.

Kaufmann, G., Wu, P., and Ivins, E. R.: Lateral viscosity variations beneath Antarctica and their implications on regional rebound motions and seismotectonics, *J. Geodyn.*, 39, 165–181, <https://doi.org/10.1016/j.jog.2004.08.009>, 2005.

Kendall, R. A., Mitrovica, J. X., and Milne, G. A.: On post-glacial sea level–II. Numerical formulation and comparative results on spherically symmetric models, *Geophys. J. Int.*, 161, 679–706, <https://doi.org/10.1111/j.1365-246X.2005.02553.x>, 2005.

King, M. A., Bingham, R. J., Moore, P., Whitehouse, P. L., Bentley, M. J., and Milne, G. A.: Lower satellite-gravimetry estimates of Antarctic sea-level contribution, *Nature*, 491, 586–589, <https://doi.org/10.1038/nature11621>, 2012.

Konrad, H., Sasgen, I., Pollard, D., and Kleemann, V.: Potential of the solid-Earth response for limiting long-term West Antarctic Ice Sheet retreat in a warming climate, *Earth Planet. Sc. Lett.*, 432, 254–264, <https://doi.org/10.1016/j.epsl.2015.10.008>, 2015.

Kustowski, B., Ekström, G., and Dziewoński, A.: Anisotropic shear-wave velocity structure of the Earth's mantle: A global model, *J. Geophys. Res.-Sol. Ea.*, 113, B06306, <https://doi.org/10.1029/2007JB005169>, 2008.

Lambeck, K., Rouby, H., Purcell, A., Sun, Y., and Sambridge, M.: Sea level and global ice volumes from the Last Glacial Maximum to the Holocene, *P. Natl. Acad. Sci. USA*, 111, 15296–15303, <https://doi.org/10.1073/pnas.1411762111>, 2014.

Larour, E., Seroussi, H., Adhikari, S., Ivins, E., Caron, L., Morlighem, M., and Schlegel, N.: Slowdown in Antarctic mass loss from solid Earth and sea-level feedbacks, *Science*, 364, eaav7908, <https://doi.org/10.1126/science.aav7908>, 2019.

Latychev, K., Mitrovica, J. X., Tromp, J., Tamisiea, M. E., Komatsitsch, D., and Christara, C. C.: Glacial isostatic adjustment on 3-D Earth models: a finite-volume formulation, *Geophys. J. Int.*, 161, 421–444, <https://doi.org/10.1111/j.1365-246X.2005.02536.x>, 2005.

Lloyd, A., Wiens, D., Zhu, H., Tromp, J., Nyblade, A., Aster, R., Hansen, S., Dalziel, I., Wilson, T., and Ivins, E.: Seismic structure of the Antarctic upper mantle imaged with adjoint tomography, *J. Geophys. Res.-Sol. Ea.*, 125, <https://doi.org/10.1029/2019JB017823>, 2020.

Lucas, E. M., Soto, D., Nyblade, A. A., Lloyd, A. J., Aster, R. C., Wiens, D. A., O'Donnell, J. P., Stuart, G. W., Wilson, T. J., Dalziel, I. W., and Winberry, J. P.: P-and S-wave velocity structure of central West Antarctica: implications for the tectonic evolution of the West Antarctic Rift System, *Earth Planet. Sc. Lett.*, 546, 116437, <https://doi.org/10.1016/j.epsl.2020.116437>, 2020.

Martín-Español, A., Zammit-Mangion, A., Clarke, P. J., Flament, T., Helm, V., King, M. A., Luthcke, S. B., Petrie, E., Rémy, F., Schön, N. and Wouters, B.: Spatial and temporal Antarctic Ice Sheet mass trends, glacio-isostatic adjustment, and surface processes from a joint inversion of satellite altimeter, gravity, and GPS data, *J. Geophys. Res.-Earth*, 121, 182–200, <https://doi.org/10.1002/2015JF003550>, 2016.

Mitrovica, J. and Forte, A.: A new inference of mantle viscosity based upon joint inversion of convection and glacial isostatic adjustment data, *Earth Planet. Sc. Lett.*, 225, 177–189, <https://doi.org/10.1016/j.epsl.2004.06.005>, 2004.

Morelli, A. and Danesi, S.: Seismological imaging of the Antarctic continental lithosphere: a review, *Global Planet. Change*, 42, 155–165, <https://doi.org/10.1016/j.gloplacha.2003.12.005>, 2004.

Morlighem, M., Rignot, E., Binder, T., Blankenship, D., Drews, R., Eagles, G., Eisen, O., Ferraccioli, F., Forsberg, R., and Fretwell, P.: Deep glacial troughs and stabilizing ridges unveiled beneath the margins of the Antarctic ice sheet, *Nat. Geosci.*, 13, 132–137, <https://doi.org/10.1038/s41561-019-0510-8>, 2020.

Nield, G. A., Barletta, V. R., Bordoni, A., King, M. A., Whitehouse, P. L., Clarke, P. J., Domack, E., Scambos, T. A., and Berthier, E.: Rapid bedrock uplift in the Antarctic Peninsula explained by viscoelastic response to recent ice unloading, *Earth Planet. Sc. Lett.*, 397, 32–41, <https://doi.org/10.1016/j.epsl.2014.04.019>, 2014.

NOAA National Geophysical Data Centre: 2-minute gridded global relief data (ETOPO2) v2, NOAA National Center for Environmental Information, <https://doi.org/10.7289/V5J1012Q>, 2006.

Nowicki, S. M. J., Payne, A., Larour, E., Seroussi, H., Goelzer, H., Lipscomb, W., Gregory, J., Abe-Ouchi, A., and Shepherd, A.: Ice Sheet Model Intercomparison Project (ISMIP6) contribution to CMIP6, *Geosci. Model Dev.*, 9, 4521–4545, <https://doi.org/10.5194/gmd-9-4521-2016>, 2016.

Paterson, W.: *Ice Sheets and Ice Shelves*, edited by: Colbeck, S., *Dynamics of Snow and Ice Masses*, Academic Press, New York, 1–78, 1980.

Pattyn, F., Perichon, L., Durand, G., Favier, L., Gagliardini, O., Hindmarsh, R. C., Zwinger, T., Albrecht, T., Cornford, S., and Docquier, D.: Grounding-line migration in plan-view marine ice-sheet models: results of the ice2sea MISMIP3d intercomparison, *J. Glaciol.*, 59, 410–422, <https://doi.org/10.3189/2013JoG12J129>, 2013.

Pollitz, F. F.: Lithosphere and shallow asthenosphere rheology from observations of post-earthquake relaxation, *Phys. Earth Planet. In.*, 293, 106271, <https://doi.org/10.1016/j.pepi.2019.106271>, 2019.

Powell, E., Gomez, N., Hay, C., Latychev, K., and Mitrovica, J.: Viscous effects in the solid Earth response to modern Antarctic ice mass flux: Implications for geodetic studies of WAIS stability in a warming world, *J. Climate*, 33, 443–459, <https://doi.org/10.1175/JCLI-D-19-0479.1>, 2020.

Powell, E., Latychev, K., Gomez, N., and Mitrovica, J. X.: The robustness of geodetically-derived 1-D Antarctic viscosity models in the presence of complex 3-D viscoelastic Earth structure, *Geophys. J. Int.*, ggac129, <https://doi.org/10.1093/gji/ggac129>, 2022.

Rignot, E., Mouginot, J., Scheuchl, B., van den Broeke, M., van Wessem, M. J., and Morlighem, M.: Four decades of Antarctic Ice Sheet mass balance from 1979–2017, *P. Natl. Acad. Sci. USA*, 116, 1095–1103, <https://doi.org/10.1073/pnas.1812883116>, 2019.

Ritsema, J., Deuss, a. A., Van Heijst, H., and Woodhouse, J.: S40RTS: a degree-40 shear-velocity model for the mantle from new Rayleigh wave dispersion, teleseismic travel-time and normal-mode splitting function measurements, *Geophys. J. Int.*, 184, 1223–1236, <https://doi.org/10.1111/j.1365-246X.2010.04884.x>, 2011.

Ritzwoller, M. H., Shapiro, N. M., Levshin, A. L., and Leahy, G. M.: Crustal and upper mantle structure beneath Antarctica and surrounding oceans, *J. Geophys. Res.-Sol. Ea.*, 106, 30645–30670, <https://doi.org/10.1029/2001JB000179>, 2001.

Schröder, L., Horwath, M., Dietrich, R., Helm, V., van den Broeke, M. R., and Ligtenberg, S. R. M.: Four decades of Antarctic surface elevation changes from multi-mission satellite altimetry, *The Cryosphere*, 13, 427–449, <https://doi.org/10.5194/tc-13-427-2019>, 2019.

Seroussi, H., Nowicki, S., Payne, A. J., Goelzer, H., Lipscomb, W. H., Abe-Ouchi, A., Agosta, C., Albrecht, T., Asay-Davis, X., Barthel, A., Calov, R., Cullather, R., Dumas, C., Galton-Fenzi, B. K., Gladstone, R., Golledge, N. R., Gregory, J. M., Greve, R., Hattermann, T., Hoffman, M. J., Humbert, A., Huybrechts, P., Jourdain, N. C., Kleiner, T., Larour, E., Leguy, G. R., Lowry, D. P., Little, C. M., Morlighem, M., Pattyn, F., Pelle, T., Price, S. F., Quiquet, A., Reese, R., Schlegel, N.-J., Shepherd, A., Simon, E., Smith, R. S., Straneo, F., Sun, S., Trusel, L. D., Van Breedam, J., van de Wal, R. S. W., Winkelmann, R., Zhao, C., Zhang, T., and Zwinger, T.: ISMIP6 Antarctica: a multi-model ensemble of the Antarctic ice sheet evolution over the 21st century, *The Cryosphere*, 14, 3033–3070, <https://doi.org/10.5194/tc-14-3033-2020>, 2020.

Shen, W., Wiens, D. A., Anandakrishnan, S., Aster, R. C., Gerstoft, P., Bromirski, P. D., Hansen, S. E., Dalziel, I. W., Heeszel, D. S., and Huerta, A. D.: The crust and upper mantle structure of central and West Antarctica from Bayesian inversion of Rayleigh wave and receiver functions, *J. Geophys. Res.-Sol. Ea.*, 123, 7824–7849, <https://doi.org/10.1029/2017JB015346>, 2018.

Shepherd, A., Gilbert, L., Muir, A. S., Konrad, H., McMillan, M., Slater, T., Briggs, K. H., Sundal, A. V., Hogg, A. E., and Engdahl, M. E.: Trends in Antarctic Ice Sheet elevation and mass, *Geophys. Res. Lett.*, 46, 8174–8183, <https://doi.org/10.1029/2019GL082182>, 2019.

Smith, B., Fricker, H. A., Gardner, A. S., Medley, B., Nilsson, J., Paolo, F. S., Holschuh, N., Adusumilli, S., Brunt, K., Csatho, B., Harbeck, K., Markus, T., Neumann, T., Siegfried, M. R., and Zwally, H. J.: Pervasive ice sheet mass loss reflects competing ocean and atmosphere processes, *Science*, 368, 1239–1242, <https://doi.org/10.1126/science.aaz5845>, 2020.

Spada, G. and Stocchi, P.: SELEN: A Fortran 90 program for solving the “sea-level equation”, *Comput. Geosci.*, 33, 538–562, <https://doi.org/10.1016/j.cageo.2006.08.006>, 2007.

Studinger, M.: IceBridge ATM L4 surface elevation rate of change, NASA National Snow and Ice Data Center Distributed Active Archive Center, Boulder, Colorado USA, 10, 2014.

The IMBIE team: Mass balance of the Antarctic Ice Sheet from 1992 to 2017, *Nature*, 558, 219–222, <https://doi.org/10.1038/s41586-018-0179-y>, 2018.

Van den Berg, J., Van de Wal, R., and Oerlemans, J.: Effects of spatial discretization in ice-sheet modelling using the shallow-ice approximation, *J. Glaciol.*, 52, 89–98, <https://doi.org/10.3189/172756506781828935>, 2006.

Van der Wal, W., Whitehouse, P. L., and Schrama, E. J.: Effect of GIA models with 3D composite mantle viscosity on GRACE mass balance estimates for Antarctica, *Earth Planet. Sc. Lett.*, 414, 134–143, <https://doi.org/10.1016/j.epsl.2015.01.001>, 2015.

Whitehouse, P. L., Gomez, N., King, M. A., and Wiens, D. A.: Solid Earth change and the evolution of the Antarctic Ice Sheet, *Nat. Commun.*, 10, 503, <https://doi.org/10.1038/s41467-018-08068-y>, 2019.

Zhao, C., King, M. A., Watson, C. S., Barletta, V. R., Bordoni, A., Dell, M., and Whitehouse, P. L.: Rapid ice unloading in the Fleming Glacier region, southern Antarctic Peninsula, and its effect on bedrock uplift rates, *Earth Planet. Sc. Lett.*, 473, 164–176, <https://doi.org/10.1016/j.epsl.2017.06.002>, 2017.

Zwinger, T., Nield, G. A., Ruokolainen, J., and King, M. A.: A new open-source viscoelastic solid earth deformation module implemented in Elmer (v8.4), *Geosci. Model Dev.*, 13, 1155–1164, <https://doi.org/10.5194/gmd-13-1155-2020>, 2020.